The Astrophysical Journal, 970:96 (29pp), 2024 July 20 https://doi.org/10.3847/1538-4357/ad3de8

The Early Ultraviolet Light Curves of Type II Supernovae and the Radii of Their Progenitor Stars

Ido Irani[1], Jonathan Morag[1], Avishay Gal-Yam[1], Eli Waxman[1], Steve Schulze[2], Jesper Sollerman[3], K-Ryan Hinds[4], Daniel A. Perley[4], Ping Chen[1], Nora L. Strotjohann[1], Ofer Yaron[1], Erez A. Zimmerman[1], Rachel Bruch[1], Eran O. Ofek[1], Maayane T. Soumagnac[5,6], Yi Yang[7,12], Steven L. Groom[8], Frank J. Masci[8], Marie Aubert[9], Reed Riddle[10], Eric C. Bellm[11], and David Hale[10]

[1] Department of Particle Physics and Astrophysics, Weizmann Institute of Science, 234 Herzl Street, 7610001 Rehovot, Israel; idoirani@gmail.com
[2] Department of Physics, The Oskar Klein Center, Stockholm University, AlbaNova, SE-10691 Stockholm, Sweden
[3] Department of Astronomy, The Oskar Klein Center, Stockholm University, AlbaNova, SE-10691 Stockholm, Sweden
[4] Astrophysics Research Institute, Liverpool John Moores University, IC2 Liverpool Science Park, 146 Brownlow Hill, Liverpool L3 5RF, UK
[5] Department of Physics, Bar Ilan University, Ramat-Gan, 52900, Israel
[6] Lawrence Berkeley National Laboratory, 1 Cyclotron Road, Berkeley, CA 94720, USA
[7] Department of Astronomy, University of California, Berkeley, CA 94720-3411, USA
[8] IPAC, California Institute of Technology, 1200 East California Boulevard, Pasadena, CA 91125, USA
[9] Université Clermont Auvergne, CNRS/IN2P3, LPC, F-63000 Clermont-Ferrand, France
[10] Caltech Optical Observatories, California Institute of Technology, Pasadena, CA 91125, USA
[11] DIRAC Institute, Department of Astronomy, University of Washington, 3910 15th Avenue NE, Seattle, WA 98195, USA
Received 2023 October 26; revised 2024 March 20; accepted 2024 March 20; published 2024 July 19

Abstract

We present a sample of 34 normal Type II supernovae (SNe II) detected with the Zwicky Transient Facility, with multiband UV light curves starting at $t \leqslant 4$ days after explosion, and X-ray observations. We characterize the early UV-optical color, provide empirical host-extinction corrections, and show that the $t > 2$ day UV-optical colors and the blackbody evolution of the sample are consistent with shock cooling (SC) regardless of the presence of "flash ionization" features. We present a framework for fitting SC models that can reproduce the parameters of a set of multigroup simulations up to 20% in radius and velocity. Observations of 15 SNe II are well fit by models with breakout radii $<10^{14}$ cm. Eighteen SNe are typically more luminous, with observations at $t \geqslant 1$ day that are better fit by a model with a large $>10^{14}$ cm breakout radius. However, these fits predict an early rise during the first day that is too slow. We suggest that these large-breakout events are explosions of stars with an inflated envelope or with confined circumstellar material (CSM). Using the X-ray data, we derive constraints on the extended ($\sim 10^{15}$ cm) CSM density independent of spectral modeling and find that most SN II progenitors lose $\dot{M} < 10^{-4} M_{\odot}\ \mathrm{yr}^{-1}$ up to a few years before explosion. We show that the overall observed breakout radius distribution is skewed to higher radii due to a luminosity bias. We argue that the 66^{+11}_{-22}% of red supergiants (RSGs) explode as SNe II with breakout radii consistent with the observed distribution of RSGs, with a tail extending to large radii, likely due to the presence of CSM.

Unified Astronomy Thesaurus concepts: Type II supernovae (1731); Core-collapse supernovae (304); Shocks (2086); Plasma astrophysics (1261); Ultraviolet astronomy (1736); Ultraviolet transient sources (1854); Transient sources (1851)

Materials only available in the online version of record: figure sets, data behind figure, machine-readable tables

1. Introduction

The progenitor stars of the majority of spectroscopically regular (Gal-Yam 2017) Type II supernovae (SNe II) are red supergiants (RSGs), as confirmed by pre-SN detections (see Smartt 2009, 2015; Van Dyk 2017, and references therein). While this is the case, we do not yet know if all RSG stars explode as SNe, and the details of the latest stages of stellar evolution are not accurately known. As we cannot know which star will explode as an SN ahead of time, the only way of systematically observing the short final stages of stellar evolution are through their terminal explosions as SNe. Using this approach, the properties of a progenitor star immediately prior to explosion can be connected to its observed SN. Connecting the progenitors to the SN explosions they create has been a long-standing goal of SN studies (Gal-Yam et al. 2007; Smartt 2015; Modjaz et al. 2019). In the last decade, large statistical studies of SNe have become commonplace. While these can place some constraints on the progenitor properties, the progenitor radius, ejected mass, and explosion energy have degenerate effects on the SN light curves (Dessart & Hillier 2019; Goldberg et al. 2019). Acquiring independent estimates of these properties through their peak and plateau properties remains a difficult and unsolved problem.

Measuring the progenitor radius is possible by observing the earliest phase of the SN explosion. The first photons emitted from the SN explosion will be the result of shock breakout of the radiation-mediated shock from the stellar surface—the breakout pulse. The photons that were captured in the shock transition region escape on a timescale of minutes to hours if

[12] Bengier-Winslow-Robertson Postdoctoral Fellow.

breakout will occur at the edge of the stellar envelope, or longer if it occurs in the surrounding circumstellar material (CSM). Typically, this allows us to constrain the progenitor radius directly from the duration of the breakout pulse (for a review of the subject, see Waxman & Katz 2017, and references therein). The shocked material, which has been compressed and heated, is then ejected and quickly reaches a state of homologous expansion (Matzner & McKee 1999). From the moment of shock breakout and in the absence of interaction with preexisting material above the photosphere, the dominant emission mechanism is the cooling of this heated envelope, which evolves according to simple analytic solutions until hydrogen recombination becomes significant.

This stage, called the shock-cooling phase, typically lasts a few days for normal SNe II and less than a day for stripped-envelope SNe and 1987A-like SNe II. During this time, the temperature and luminosity evolution are highly sensitive to the progenitor radius and the shock velocity, allowing one to constrain these parameters (Chevalier 1992; Nakar & Sari 2010; Rabinak & Waxman 2011). Since the first generation of models, theoretical advancements have extended the applications of shock-cooling models to low-mass envelopes (Piro 2015; Piro et al. 2021) and later times (Sapir & Waxman 2017). Recently, Morag et al. (2023, hereafter M23) interpolated between the planar and spherical phases, extending the validity of the model of Sapir & Waxman (2017) to earlier times, and treated the suppression of flux in UV due to line absorption and emission (Morag et al. 2024, hereafter M24). This model, as well as its predecessors, is valid prior to hydrogen recombination at 0.7 eV.

In the past decade, high-cadence and wide-field surveys have enabled the early-time detection and multiband follow-up of SNe. The Palomar Transient Factory (Law et al. 2009; Kulkarni 2013), the Asteroid-Terrestrial impact Last Alert System (Tonry et al. 2018), the Zwicky Transient Facility (ZTF; Bellm et al. 2019; Graham et al. 2019), the Distance Less than 40 Mpc Survey (Tartaglia et al. 2018), and, most recently, the Young Supernovae Experiment (Jones et al. 2021) have been conducting 1–3 day cadence wide-field surveys and regularly detect early-phase SNe (e.g., Hachinger et al. 2009; Arcavi et al. 2011; Gal-Yam et al. 2011, 2014, 2022; Nugent et al. 2011; Ben-Ami et al. 2014; Khazov et al. 2016; Yaron et al. 2017; Hosseinzadeh et al. 2018, 2022; Ho et al. 2019; Soumagnac et al. 2020; Bruch et al. 2021; Jacobson-Galán et al. 2022; Perley et al. 2022; Terreran et al. 2022; Tinyanont et al. 2022; Irani et al. 2024a).

Previous attempts to model the early-phase emission of SNe II yielded mixed results. Many studies fit the analytical shock-cooling models of Nakar & Sari (2010) or Rabinak & Waxman (2011). These models require multiband photometry extending to the early time and the UV, as the model parameters are highly sensitive to the temperature ∼1 day after explosion. Many works find radii that are small compared to the observed RSG distribution from the Small and Large Magellanic Clouds. For example, González-Gaitán et al. (2015) and Gall et al. (2015) compile large optical light-curve samples, fitting *ugriz*- and *r*-band photometry, respectively, and assume a fixed validity time for the models (i.e., not dependent on the model parameters). While Rubin et al. (2016) and Rubin & Gal-Yam (2017) demonstrated that adopting a fixed validity domain introduces a bias in the parameter inference, assuming a fixed validity domain remains commonplace in the literature (e.g., Hosseinzadeh et al. 2018). Recent attempts by Soumagnac et al. (2020), Ganot et al. (2022), and Hosseinzadeh et al. (2023) find large RSG radii of $\sim 1000\,R_{\odot}$ by fitting early UV-optical light curves, in tension with previous results, while Vallely et al. (2021) fit single-band high-cadence Transiting Exoplanet Survey Satellite (TESS; Ricker et al. 2014) light curves and find unrealistically small RSG progenitor radii, which they calibrate to numerical simulations.

While some large samples by Valenti et al. (2016) and Faran et al. (2017) fit the luminosities and temperatures of SNe II using multiband UV-optical data sets, these did not extend to the very early times. However, these studies demonstrate that the blackbody evolution is in agreement with the expectations of the shock-cooling framework of a cooling blackbody with $T \sim t^{-0.5}$ (Faran et al. 2017).

A different approach to analytic cooling models is the use of numerical hydrodynamical simulations. Motivated by the fact that narrow features from CSM interaction are commonly observed in SNe II (Gal-Yam et al. 2014; Khazov et al. 2016; Yaron et al. 2017; Bruch et al. 2021, 2023), these models include a dense shell of CSM, ejected from the progenitor before explosion. This results in an extended nonpolytropic density profile extending to a few 10^{14} cm from the progenitor star prior to explosion. Morozova et al. (2018) show that the early-time multiband evolution of a sample of SNe II is better explained by models with dense CSM compared to models that do not include CSM. The breakout radii in this case are typically at the edge of the CSM, at large radii ($\lesssim 3000\,R_{\odot}$). Dessart et al. (2017) and Dessart & Hillier (2019) fit the early (>a few days) spectroscopic and photometric sequence of SNe with a grid of non–local thermal equilibrium (LTE) simulations and find that a small amount of CSM improves the match of the models with the early-time photometry. Förster et al. (2018) fit a sample of 26 (photometrically classified) SNe II to a grid of hydrodynamical models and argue that they observe a delayed rise in the majority of SNe II explained by the presence of CSM.

In this paper, we present a sample of spectroscopically regular SNe II with well-sampled UV-optical light curves. We present our sample selection strategy in Section 2 and the details of our photometric and X-ray follow-up in Section 3. In Section 4, we analyze the color evolution (Section 4.1) and blackbody evolution (Section 4.2) of the SNe. In Section 4.3, we model the light curves during the shock-cooling phase. We discuss our results and their implications for the SN progenitors in Section 5.

Throughout the paper, we use a flat ΛCDM cosmological model with $H_0 = 67.4\,\mathrm{km\ s^{-1}\,Mpc^{-1}}$, $\Omega_M = 0.315$, and $\Omega_\Lambda = 0.685$ (Planck Collaboration et al. 2018).

2. Sample

2.1. Observing Strategy

In Bruch et al. (2021), we described the selection process of infant SNe from the ZTF alert stream. Using a custom filter, we select transients in extragalactic fields ($|b| > 14°$), with a nondetection limit of <2.5 days from the first detection, and from a nonstellar origin. These candidates are routinely manually inspected by a team of duty astronomers in Europe and Israel during California nighttime in order to reject false positives (such as stellar flares, galactic transients, and active galactic nuclei). Management of follow-up resources and candidates was performed through the GROWTH marshal (Kasliwal et al. 2019) and Fritz/`SkyPortal` platforms (van der Walt et al. 2019; Coughlin et al. 2023). Promising candidates rising by at least 0.5 mag from the previous nondetection are followed up with optical spectroscopy, optical

Table 1
List of 34 SNe Included in This Study

SN	ZTF ID	α (J2000)	δ (J2000)	z	d[a] (Mpc)	t_{ND} (JD)	t_{exp} (JD)	τ_{flash}[b] (days)	Reference
SN 2018cxn	ZTF18abckutn	237.026897	55.714855	0.0401	186.6	2458289.7490	2458289.76 ± 0.01	<0.0	1
SN 2018dfc	ZTF18abeajml	252.032360	24.304095	0.0365	170.0	2458302.7103	2458303.8 ± 0.009	6.2 ± 2.8	1
SN 2018fif	ZTF18abokyfk	2.360629	47.354083	0.0172	76.5	2458349.8973	2458350.874 ± 0.002	1.6 ± 1.0	1, 2
SN 2019eoh	ZTF19aatqzim	195.955635	38.289155	0.0501	229.6	2458601.7817	2458606.683 ± 0.031	<0.0	3
SN 2019gmh	ZTF19aawgxdn	247.763189	41.153961	0.0307	141.3	2458633.8250	2458634.324 ± 0.444	<1.4	3
SN 2019nvm	ZTF19abqhobb	261.411100	59.446730	0.0181	86.4	2458713.7416	2458714.69 ± 0.007	1.9 ± 1.0	3, 4
SN 2019omp	ZTF19abrlvij	260.142987	51.632780	0.0450	206.9	2458717.7910	2458718.713 ± 0.0	<0.0	3
SN 2019oxn	ZTF19abueupg	267.803290	51.382550	0.0200	90.3	2458723.7895	2458724.342 ± 0.129	<0.4	3
SN 2019ozf	ZTF19abulrfa	279.817010	54.287872	0.0480	221.2	2458723.7900	2458724.728 ± 0.005	<0.0	3
SN 2019ust	ZTF19acryurj	13.593396	31.670182	0.0220	96.0	2458799.8053	2458800.04 ± 0.177	5.0 ± 0.5	3
SN 2019wzx	ZTF19aczlldp	37.782326	4.311291	0.0275	124.9	2458833.7282	2458835.506 ± 0.092	<1.1	11
SN 2020cxd	ZTF20aapchqy	261.621953	71.094063	0.0039	23.7	2458896.0296	2458896.671 ± 0.671	<2.4	5, 6
SN 2020dyu	ZTF20aasfhia	184.913047	33.040393	0.0500	230.7	2458911.9254	2458912.814 ± 0.021	<0.0	3
SN 2020fqv	ZTF20aatzhhl	189.138576	11.231654	0.0075	15.0	2458936.9007	2458939.43 ± 0.16	<0.9	7
SN 2020jfo	ZTF20aaynrrh	185.460355	4.481697	0.0052	14.7	2458971.7751	2458975.231 ± 0.424	<0.5	8
SN 2020lfn	ZTF20abccixp	246.737033	20.245906	0.0440	202.2	2458995.8154	2458996.701 ± 0.018	4.2 ± 1.5	3
SN 2020mst	ZTF20abfcdkj	281.793965	60.496802	0.0590	274.0	2459012.8161	2459013.689 ± 0.067	<0.1	3
SN 2020nif	ZTF20abhjwvh	196.057282	−10.351002	0.0104	50.5	2459021.7334	2459023.783 ± 0.765	<0.9	11
SN 2020nyb	ZTF20abjonjs	29.783900	86.676205	0.0155	72.1	2459026.9709	2459033.849 ± 0.014	<0.0	11
SN 2020pni	ZTF20ablygyy	225.958184	42.114032	0.0169	83.2	2459045.7542	2459046.638 ± 0.004	5.0 ± 1.0	9
SN 2020pqv	ZTF20abmoakx	220.498180	8.462724	0.0338	160.2	2459046.7104	2459048.646 ± 0.023	5.2 ± 2.5	3
SN 2020qvw	ZTF20abqkaoc	250.983335	77.879897	0.0500	230.7	2459065.8438	2459066.222 ± 0.417	<0.6	11
SN 2020afdi	ZTF20abqwkxs	224.868111	73.898678	0.0239	110.9	2459069.7995	2459070.277 ± 0.341	1.3 ± 0.5	3
SN 2020ufx	ZTF20acedqis	322.652706	24.673752	0.0500	230.7	2459116.8338	2459117.752 ± 0.015	4.9 ± 1.0	3
SN 2020uim	ZTF20acfdmex	28.188740	36.623160	0.0185	80.5	2459117.8602	2459118.823 ± 0.0	<0.1	3
SN 2020xhs	ZTF20acknpig	30.742868	45.020286	0.0244	106.6	2459138.8669	2459138.936 ± 0.301	<1.8	3
SN 2020xva	ZTF20aclvtnk	263.035128	53.653989	0.0240	108.7	2459141.7258	2459142.69 ± 0.69	<1.0	3
SN 2020aavm	ZTF20acrinvz	116.681975	18.113551	0.0450	227.2	2459168.9788	2459169.935 ± 0.746	<1.0	11
SN 2020abue	ZTF20acvjlev	121.084598	56.302082	0.0280	126.9	2459188.0078	2459189.663 ± 0.118	<0.2	11
SN 2020acbm	ZTF20acwgxhk	40.074159	2.427067	0.0217	93.1	2459192.7093	2459193.654 ± 0.022	<0.1	11
SN 2021apg	ZTF21aafkwtk	205.330192	24.495531	0.0269	128.4	2459228.0064	2459230.722 ± 0.186	<1.2	11
SN 2021ibn	ZTF21aasfseg	132.558710	37.026990	0.0442	197.2	2459306.7862	2459307.252 ± 0.295	<0.4	11
SN 2021skn	ZTF21abjcjmc	246.204167	39.734653	0.0297	139.5	2459397.8203	2459398.735 ± 0.743	<1.1	11
SN 2021yja	ZTF21acaqdee	51.088215	−21.565626	0.0053	22.6	2459459.4000	2459464.4 ± 0.06	<2.3	10

References. (1) Bruch et al. (2021); (2) Soumagnac et al. (2020); (3) Bruch et al. (2023); (4) Vallely et al. (2021); (5) Yang et al. (2021); (6) Valerin et al. (2022); (7) Tinyanont et al. (2022); (8) Sollerman et al. (2021); (9) Terreran et al. (2022); (10) Hosseinzadeh et al. (2022); (11) TNS classification reports: Perley (2019), Dahiwale & Fremling (2020a), Dahiwale & Fremling (2020b), Hiramatsu et al. (2020), Perley et al. (2020a), Pessi et al. (2020), Weil et al. (2020), Deckers et al. (2021), Delgado et al. (2021), Siebert et al. (2021).

[a] Corrected for Virgo, Great Attractor, and Shapley supercluster infall.

[b] In rest-frame days, calculated using the last spectrum showing flash features or by taking the first spectrum as an upper limit.

(This table is available in machine-readable form in the online article.)

photometry (various instruments), and UV photometry using the UV-Optical Telescope (UVOT) on board the Neil Gehrels Swift Observatory (Gehrels et al. 2004; Roming et al. 2005). We also followed-up publicly announced infant SNe II that passed our criteria with ZTF data during the first week. While we initially required a blue color $g-r<0$ mag for triggering UVOT, this assumption was later relaxed. For this paper, we consider all ZTF infant SNe with UV photometry in the first 4 days after estimated explosion and that are classified as spectroscopically regular SNe II at peak light. We consider SNe that are detected until 2021 December 31. Classification references are listed in Table 1.

2.2. Distance

We adopt Hubble-flow distances using the NASA Extragalactic Database[13] and using their online calculator to correct the redshift distance for Virgo, Great Attractor, and Shapley supercluster infall (based on the work of Mould et al. 2000). The top panel of Figure 1 shows the distribution of distances in our sample compared to that of a magnitude-limited and spectroscopically complete sample from the ZTF Bright Transient Survey (BTS; Fremling et al. 2020; Perley et al. 2020b).[14]

2.3. Extinction

We correct for foreground Galactic reddening using the Schlafly & Finkbeiner (2011) recalibration of the Schlegel et al. (1998) extinction maps and assuming a Cardelli et al. (1989) Milky Way extinction law with $R_V=3.1$. These corrections are applied to all photometry data appearing in this paper. We do

[13] https://ned.ipac.caltech.edu/

[14] http://sites.astro.caltech.edu/ztf/rcf/explorer.php

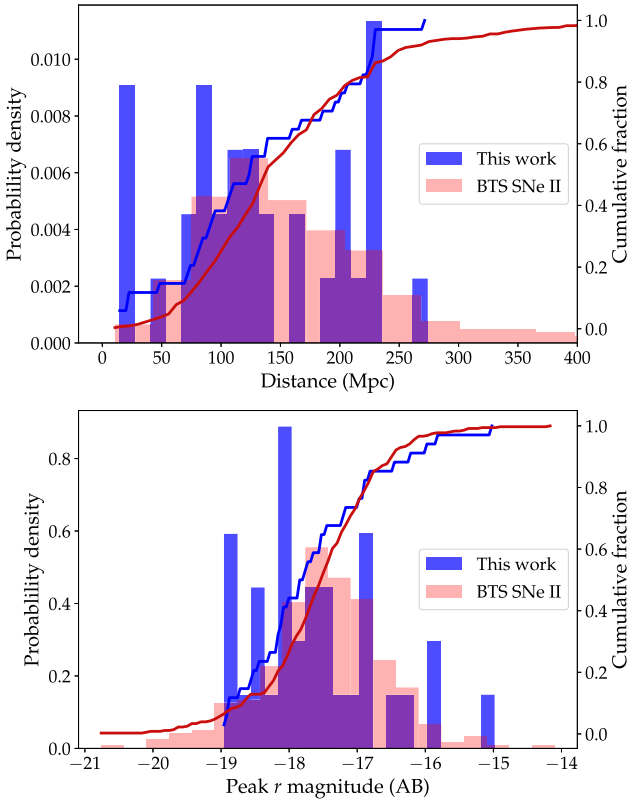

Figure 1. In the top panel, we show the distribution of distances to the SNe in our sample, compared to the distribution of BTS SNe II. We truncate the plot at 400 Mpc for clarity. In the bottom panel, we show the distribution of peak r-band magnitude compared to BTS SNe II. In both panels, we show histograms and the cumulative distributions.

not correct the photometry for host-galaxy extinction and treat this effect separately in Section 4.3.

2.4. Time of Zero Flux

We acquire an initial estimate of the time of zero flux t_0 using a power-law extrapolation of the forced-photometry flux to 0. Using both g-band and r-band data, we fit a function $f_\lambda = f_0 (t - t_0)^n$ with a slope of $0 < n < 5$ and allow values of t_0 between the first detection of the SN and the last nondetection. We then estimate the error on t_0 as the scatter in $t_{0,\mathrm{best}}$ over all allowed values of n and choose to use the band with the best constraint on t_0. In Figure 2, we show the distribution of detection times in both UV and optical bands relative to the estimated time of zero flux computed from optical data. We find that a large fraction of the SNe have t_0 close to their first detections. Most of these are SNe where first detections in the forced-photometry light curve are recovered from a nondetection in the automated ZTF alert photometry, resulting in a sharp rise and t_0 estimates that are very close to the time of first detection. As the SN time of zero flux should not correlate with the time of first detection, we expect a uniform distribution in t_0 and t_{first}. $t_{\mathrm{first}} - t_0$ should then be a rising and falling distribution. The fact that our results deviate from such a distribution indicates a systematic deviation from a power-law rise in flux—a model that is not physically motivated. Hosseinzadeh et al. (2023) fit the early light curve of the recently discovered Type II SN 2023ixf (Itagaki 2023) and show that the rise is comprised of two phases: a slower phase followed by a sharply rising phase. For such a light

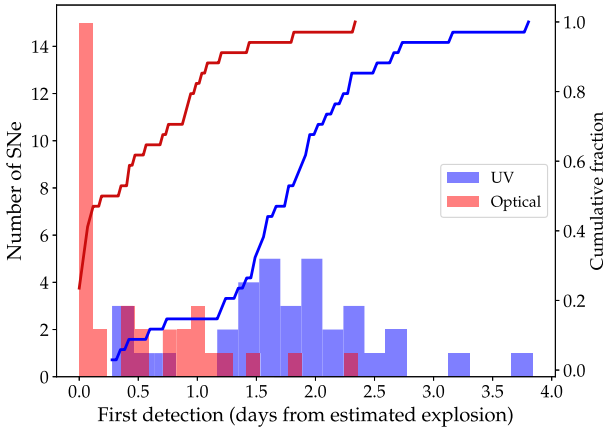

Figure 2. The times of first detection relative to the estimated time of zero flux in the UV and optical bands. Both a histogram and a cumulative distribution are shown.

curve, extrapolating based on the sharply rising phase would result in a time of first light too late by several hours, and the first point on the rise would be close to the fit t_0. Our fit provides preliminary evidence that this is the case for the majority of SNe II.

2.5. Flash Feature Timescale

Bruch et al. (2021) define flash features based on the presence of the λ4686 He II feature before broad H recombination features appear. The flash feature duration τ_{flash} is defined through the half-time between the last spectrum showing λ4686 He II emission and the subsequent epoch (Bruch et al. 2023). We adopt these definitions and the measurements of Bruch et al. (2023) throughout our paper. We extend the estimation to the SNe not included in Bruch et al. (2023) using all available spectroscopy, which will be released in a future publication.

In Table 1, we list the 34 SNe in our sample, as well as their median alert coordinates, redshifts, distance estimates, nondetection limits, estimated time of zero flux, and flash feature timescales, if applicable.

2.6. RSG Radiation-hydrodynamical Simulations

When comparing data to semianalytic models, which are calibrated to numerical simulations, it is unclear how the calibration scatter and theoretical uncertainties will propagate to observed fluxes. These could potentially manifest as correlated residuals when the model is compared to the data and subsequently create biases in the fit parameters. In order to demonstrate and account for such effects in our analysis, we repeat some of the analyses we perform throughout the paper with a set of 28 multigroup radiation-hydrodynamical simulations of RSGs described in detail in M24. These simulations are generated by relaxing the assumption of LTE and instead solving the radiation transfer using multiple photon groups and a realistic opacity table with free–free, bound–free, and bound–bound opacities at different densities, temperatures, and compositions. Thus, these simulations account for the effects of line blanketing and line emission. The simulations allow us to generate synthetic data sets with arbitrary sampling in time with any set of filters. Unless mentioned otherwise, we use the sampling, filters, and error bars of the light curves of SN 2020uim, arbitrarily chosen from our sample as a

representative SN. We do not add simulated noise, and all points are assumed to be detected regardless of luminosity unless otherwise mentioned.

3. Observations

3.1. Optical Photometry

ZTF photometry in the *gri* bands was acquired using the ZTF camera (Dekany et al. 2020) mounted on the 48 inch (1.2 m) Samuel Oschin Telescope at Palomar Observatory. These data were processed using the ZTF Science Data System (Masci et al. 2019).

While scanning was preformed using the automated alert photometry pipeline, the light curves reported in this work were obtained using the ZTF forced-photometry service.[15] The forced photometry is performed on difference images produced using the optimal image-subtraction algorithm of Zackay, Ofek, and Gal-Yam (Zackay et al. 2016) at the position of the SN, calculated from the median ZTF alert locations that are listed in Table 1. We removed images that have flagged difference images (with problems in the subtraction process), bad pixels close to the SN position, a large standard deviation in the background region, or a seeing of more than 4″. We performed a baseline correction to ensure the mean of the pre-SN flux is 0. We report detections above a 3σ threshold and use a 5σ threshold for upper limits.

In addition to the ZTF photometry, we also used the following instruments to collect early multiband light curves.

1. The Optical Imager (IO:O) at the 2.0 m robotic Liverpool Telescope (LT; Steele et al. 2004) at the Observatorio del Roque de los Muchachos. We used the Sloan Digital Sky Survey (SDSS; York et al. 2000) *u*, *g*, *r*, *i*, and *z* filters. Reduced images were downloaded from the LT archive and processed with custom image-subtraction and analysis software (K. Hinds and K. Taggart et al. 2024, in preparation). Image stacking and alignment are performed using `SWarp` (Bertin 2010) where required. Image subtraction is performed using a preexplosion reference image in the appropriate filter from the Panoramic Survey Telescope and Rapid Response System 1 (Pan-STARRS1; Chambers et al. 2016) or SDSS. The photometry is measured using point-spread function (PSF) fitting methodology relative to Pan-STARRS1 or SDSS standards and is based on techniques in Fremling et al. (2016). For SDSS fields without *u*-band coverage, we returned to these fields after the SN had faded on photometric nights to create deep stacked *u*-band reference imaging. We then calibrated these field using IO:O standards taken on the same night at varying air masses and used these observations to calibrate the photometry (Smith et al. 2002).
2. The Rainbow Camera (Blagorodnova et al. 2018) on the Palomar 60 inch (1.5 m) telescope (Cenko et al. 2006). Reductions were performed using the automatic pipeline described by Fremling et al. (2016).

In addition to the above, we use early optical light curves from the literature. These include the multiband light curves covering the rise of SN 2021yja (Hosseinzadeh et al. 2022) and light curves from TESS for SN 2020fqv (Tinyanont et al. 2022) and SN 2020nvm (Vallely et al. 2021).

[15] See ztf_forced_photometry.pdf under https://irsa.ipac.caltech.edu/data/ZTF/docs.

3.2. UV Photometry

UV photometry was acquired for all SNe using UVOT on board the Neil Gehrels Swift Observatory (Gehrels et al. 2004; Roming et al. 2005). We reduced the images using the Swift `HEAsoft`[16] tool set. Individual exposures comprising a single visit were summed using `uvotimsum`. Source counts were then extracted using `uvotsource` from the summed images using a circular aperture with a radius of 5″. The background was estimated from several larger regions surrounding the host galaxy. These counts were then converted to fluxes using the photometric zero-points of Breeveld et al. (2011) with the latest calibration files from 2020 September and including a small-scale sensitivity correction with the latest map of reduced sensitivity regions on the sensor from 2022 March. A UV template image was acquired for all SNe and for all bands after the SN had faded, with an exposure time twice as long as used for the deepest image of the SN. These images were then summed with any archival images of the site and used to estimate the host flux at the SN site. We remove the local host-galaxy contribution by subtracting the SN site flux from the fluxes of the individual epochs. In Figure 3, we show the early *g*, *r*, and UVW2 light curves of the SNe in our sample. In Figure 4, we show a representative example of the multiband light curves in our sample. We make the multiband light-curve figures of individual SNe available through WISeREP. Finally, we show the full ZTF forced-photometry light curves in Figure 23.

3.3. X-Ray Observations

While the SNe were monitored with UVOT, Swift also observed the field between 0.3 and 10 keV with its onboard X-Ray Telescope (XRT) in photon-counting mode (Burrows et al. 2005). We analyzed these data with the online tools provided by the UK Swift team.[17] These online tools use the methods of Evans et al. (2007, 2009) and the software package `HEASoft` v. 6.29 to generate XRT light curves and upper limits, perform PSF fitting, and provide stacked images.

In most cases, the SNe evaded detection at all epochs. We derive upper limits by calculating the median 3σ count-rate limit of each observing block in the 0.3–10 keV band, determined from the local background. We stack all data (acquired during UV observations of the SNe at early times and when creating the UV templates), converting the count rates to unabsorbed flux by assuming a power-law spectrum with a photon index of 2 and taking into account the Galactic neutral hydrogen column density at the location of the SN (HI4PI Collaboration et al. 2016).

In several cases (SN 2020jfo, SN 2020nif, and SN 2020fqv), we find spurious detections that are likely associated with a nearby constant source, identified by inspecting coadded X-ray images over all epochs and by comparing to archival survey data through the HILIGT server (Saxton et al. 2022). We treat the measured flux as upper limits on the SN flux.

For SN 2020acbm and SN 2020uim, we report $>3\sigma$ X-ray detections from the binned exposures.[18] For both SNe, the SN

[16] https://heasarc.gsfc.nasa.gov/docs/software/heasoft/ v. 6.26.1.

[17] https://www.swift.ac.uk/user_objects

[18] We note that while the detection significance $S/\sqrt{(B)} > 3$, where S is the source flux and B is the background level, taking into account the source flux in the error calculation results in a $<3\sigma$ measurement error, since the measurement signal-to-noise is $S/\sqrt{(B+S)}$. These approximations for the signal-to-noise hold in the Gaussian limit, which is approximately correct in our case.

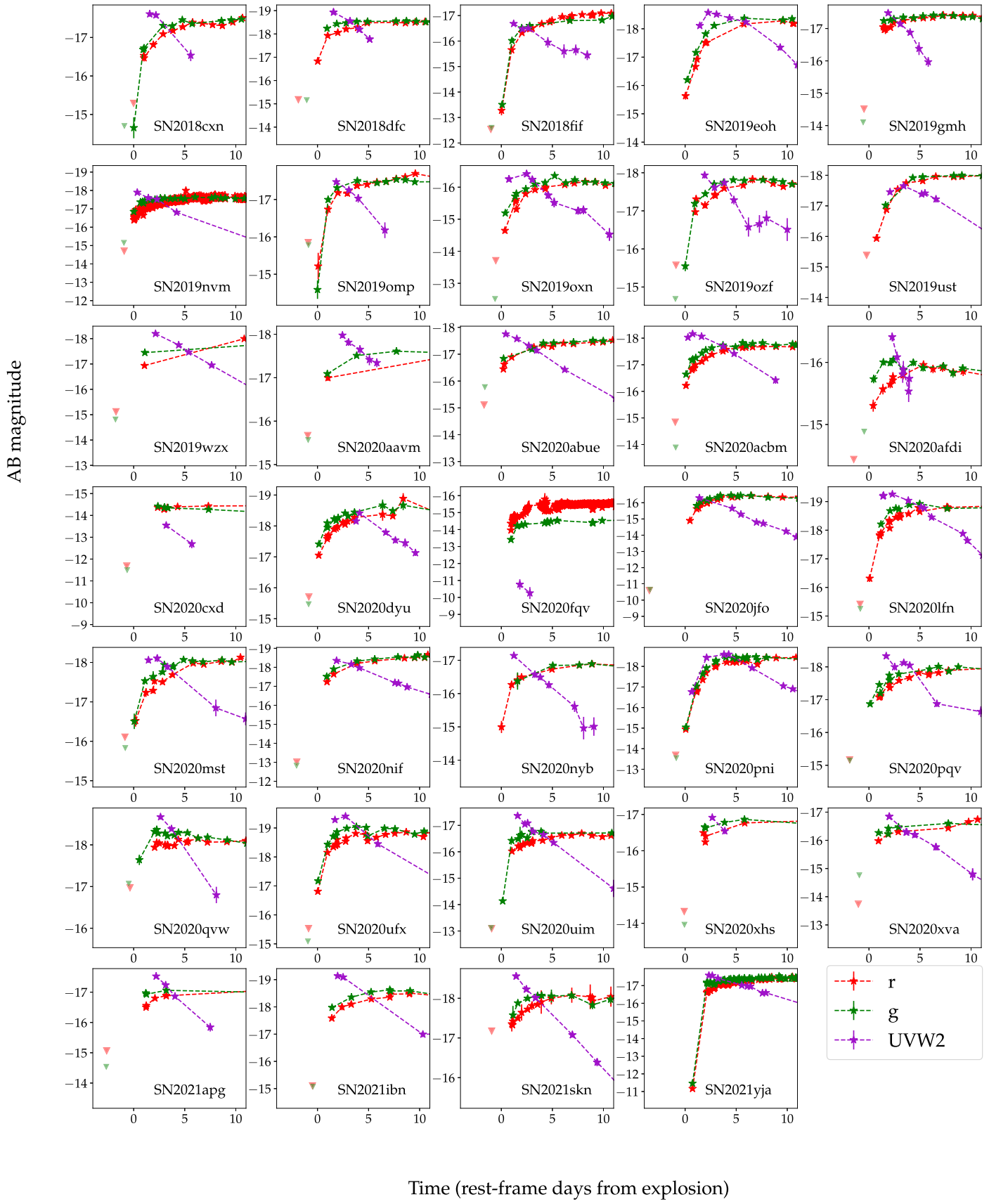

Figure 3. UVW2 (magenta stars), *g* (green stars), and *r* (red stars) light curves for all of the objects in our samples. The latest upper limits before discovery are marked with a downward-facing triangle. We note that some points that are marked as limits in the alert photometry became detections using forced photometry.

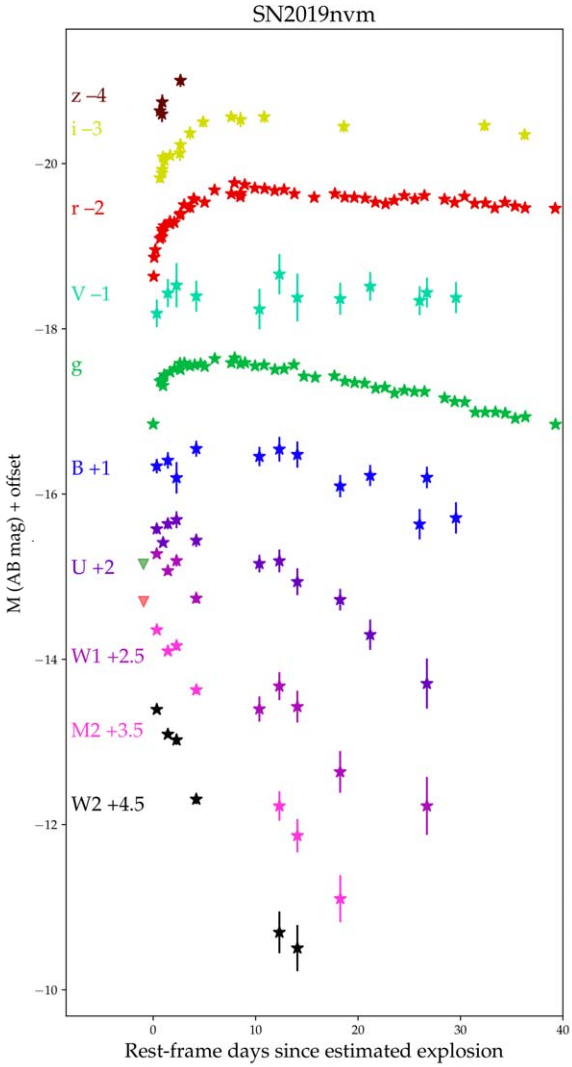

Figure 4. A representative example of the multiband light curves of SN 2019nvm in the first 40 days. The photometry is also available as the data behind the figure.

(The data used to create this figure are available in the online article.)

(The complete figure set (34 images) is available in the online article.)

location is within the 90% error region of the source PSF. In the case of SN 2020pqv, we report a detection 11″ from the SN where the source 90% localization region is 8.″5. We lack constraining limits on the quiescent flux at the location of all three SNe when comparing to archival ROSAT data or compared to the late-time XRT exposures. For SN 2021yja, we report a source 2.″6 from the SN site from observations in the first 10 days, brighter by a factor of 4.2 ± 1.8 than the derived 3σ upper limit from observation in subsequent epochs, robustly indicating that the emission is related to the SN. We report our measurements in Table 2 and show our results in Figure 5.

4. Results

4.1. Color Evolution

Before recombination begins, and although the external layers of the SN ejecta are not in LTE, the spectrum of an SN II is expected to be well approximated by a blackbody (Baron et al. 2000; Blinnikov et al. 2000; Nakar & Sari 2010; Rabinak & Waxman 2011; M24). However, several reasons exist to expect deviations of the spectrum from a perfect blackbody.

1. Extinction can contribute significantly to deviations from a blackbody. While the exact applicable extinction law has a modest effect on the optical colors, it can create major differences in the UV and UV-optical colors. Large R_V values will cause bluer UV-optical colors compared to an $R_V = 3.1$ Milky Way extinction law. Many star-forming galaxies lack the characteristic "bump" at 220 nm, which will mostly affect the UVM2-band photometry (Calzetti et al. 2000; Salim & Narayanan 2020). For both SNe Ia and stripped-envelope SNe, sample color curves have been used to derive a "blue edge" where the amount of extinction is assumed to be zero (Phillips et al. 1999; Stritzinger et al. 2018). This in turn has been used to estimate the host-galaxy extinction in the line of sight to the SN, typically performed at phases for which the intrinsic scatter in color is minimal.
2. While a frequency-independent opacity is expected to yield a blackbody continuum, a frequency-dependent opacity will create deviations. These will manifest as emission and absorption features—particularly line blanketing in the UV, as well as broad deviations from the blackbody in the continuum. These effects strongly depend on the temperature of the ejecta. M24 characterize these deviations using multigroup radiation-hydrodynamical simulations including line opacity and confirmed against a separate high frequency resolution ($\Delta\lambda/\lambda \sim 10^{-5}$) calculation that incorporates Doppler expansion opacity. These effects are included in their latest analytical model. Line blanketing in the UV is observed in the few early-time UV spectra of SNe II (Brown et al. 2007; Vasylyev et al. 2022, 2023; Bostroem et al. 2023a; Zimmerman et al. 2024). Recently, Zimmerman et al. (2024) confirmed the presence of emission lines from highly ionized species in the UV, as well as photospheric absorption features that appear in the UV while the optical spectrum is still a smooth continuum around $T \sim 15{,}000$ K.
3. CSM interaction is suggested to create bluer UV-optical colors and to be associated with a higher luminosity and with spectral signatures indicating the presence of CSM (Ofek et al. 2010; Chevalier & Irwin 2011; Katz et al. 2011; Hillier & Dessart 2019). CSM interaction is typically accompanied by strong line emission (Yaron et al. 2017), possibly in the UV, which can create deviations from the blackbody.

Using our well-sampled light curves, we constrain the deviations from a blackbody spectral energy distribution (SED) in our sample, as well as attempt to isolate their main source (i.e., physical or extinction).

First, we consider the effect of extinction. In Figure 6, we show the UVW2 − r and UVW2 − UVW1 color curves for our sample. On both plots, we illustrate the effect of applying galactic extinction with $E(B-V)$ of 0.2 and 0.4 mag with red and black arrows, respectively. The dashed lines show the expected colors of a blackbody with various temperatures in the background. The scatter in the color curves represents the variance in temperature and extinction. A significant variance

Table 2
XRT Photometry for SNe Included in This Study

SN	t (days)[a]	t_{max} (days)[a]	t_{min} (days)[a]	XRT Count Rate[b] (s^{-1})	Flux[c] (10^{-14} erg s^{-1} cm^{-2})	Luminosity[c] (10^{40} erg s^{-1})
SN 2018cxn	7.2	10.0	1.6	<0.002	<7.1	<28.3
SN 2018dfc	1.5	5.2	1.5	<0.0011	<4.3	<14.08
SN 2018fif	2.1	16.8	1.2	<0.0015	<6.4	<4.56
SN 2019eoh	11.6	20.0	1.4	<0.0015	<5.3	<33.68
SN 2019gmh	479.9	480.4	1.9	<0.0009	<3.2	<7.41
SN 2019nvm	7.6	230.2	0.3	<0.0006	<2.3	<1.85
SN 2019omp	2.6	11.2	1.8	<0.0019	<6.9	<35.07
SN 2019oxn	2.3	10.6	0.7	<0.0018	<6.8	<6.6
SN 2019ozf	196.6	391.3	1.9	<0.0005	<1.9	<10.9
SN 2019ust	20.5	325.5	2.1	<0.0005	<2.2	<2.55
SN 2019wzx	28.7	692.5	2.1	<0.0008	<2.9	<5.39
SN 2020aavm	4.3	6.2	2.4	<0.0016	<6.2	<31.65
SN 2020abue	1.7	11.3	0.4	<0.0018	<7.0	<13.45
SN 2020acbm	5.7	22.8	0.3	0.0011 ± 0.0004	4.0 ± 1.5	4.56 ± 1.71
SN 2020afdi	3.2	4.0	2.3	<0.0027	<10.1	<14.05
SN 2020cxd	5.0	14.9	2.9	<0.0028	<10.7	<0.38
SN 2020dyu	9.6	476.7	2.3	<0.0008	<2.9	<18.22
SN 2020fqv[d]	1.7	59.0	0.0	<0.0072	<43.1	<5.79
SN 2020jfo[d]	1.4	84.5	0.0	<0.0017	<6.3	<0.41
SN 2020lfn	4.0	119.5	1.4	<0.0004	<1.7	<8.03
SN 2020mst	2.4	13.5	1.4	<0.0013	<5.2	<46.13
SN 2020nif[d]	3.3	16.8	0.0	<0.006	<22.9	<5.87
SN 2020nyb	4.2	12.3	1.2	<0.0012	<5.3	<3.05
SN 2020pni	6.9	103.1	0.6	<0.0006	<2.1	<1.41
SN 2020pqv	12.6	31.3	1.5	0.0005 ± 0.0002	1.8 ± 0.9	5.2 ± 2.42
SN 2020qvw	3.7	484.5	2.6	<0.0016	<6.2	<39.45
SN 2020ufx	2.7	267.2	1.7	<0.0007	<2.8	<17.74
SN 2020uim	272.2	272.5	272.0	<0.0036	<14.7	<12.14
SN 2020uim	10.0	271.8	1.6	0.0008 ± 0.0004	3.1 ± 1.5	2.6 ± 1.26
SN 2020xhs	17.5	256.7	2.6	<0.0014	<6.3	<9.06
SN 2020xva	2.0	18.3	1.9	<0.0009	<3.5	<4.92
SN 2021apg	8.1	14.3	1.9	<0.0014	<4.8	<8.53
SN 2021ibn	129.6	257.3	1.9	<0.0008	<2.8	<13.54
SN 2021skn	2.8	12.1	1.4	<0.0015	<5.4	<11.68
SN 2021yja	4.3	8.0	2.3	0.0013 ± 0.0003	4.8 ± 1.2	0.32 ± 0.08
SN 2021yja	46.9	83.2	15.9	<0.0006	<2.1	<0.14

Notes.
[a] All times are reported in rest-frame days.
[b] We report 3σ upper limits, or measurements with a significance of 3σ above the background level.
[c] Fluxes are corrected for galactic neutral hydrogen column density and converted from count rates assuming a power-law spectrum with a photon index of 2.
[d] For SN 2020jfo, SN 2020fqv, and SN 2020nif, we report quiescent host-galaxy detections as upper limits on the SN flux.

(This table is available in machine-readable form in the online article.)

in temperature (and thus in color) is expected if these SNe are powered by shock cooling, as the temperature evolution is sensitive to the shock-breakout radius. Despite this, all SNe in our sample besides the highly extinguished SN 2020fqv (Tinyanont et al. 2022) fall within $E(B-V)=0.2$ mag of the bluest SN in the sample. We consider this value an upper limit on the reddening affecting these SNe.[19]

In Figure 7, we show the $M_n - M_r$ color distributions in our sample at $t=2$ and $t=4$ days (panels (a) and (b), respectively), where $n \in \{\mathrm{UVW2}, \mathrm{UVM2}, \mathrm{UVW1}, U, g, i\}$. For each band, the transparent data points show the interpolated color, the filled diamonds and black dashed lines show the average color, and the error bars and gray shaded regions show the standard deviation of the color. An extinction corresponding to a galactic extinction curve with $E(B-V)=0.2$ mag applied to the bluest SN in the UVW2 $-$ r color (transparent points with the highest $M_n - M_r$) is indicated by the gray transparent data points. For the UVW2 $-$ r and UVM2 $-$ r colors, which are most sensitive to extinction, this mild amount of extinction is sufficient to account for the full scatter in all SNe besides SN 2020fqv. However, since $E(B-V)=0.2$ mag is not enough to account for the optical scatter (as indicated by the trend of the gray line), it is likely that this scatter is explained by differences in temperature and that the typical extinction of the sample is lower. Assuming that SN 2020fqv is well represented by our sample in its intrinsic SED, we use the average colors to calculate its extinction curve. In each curve, we determine $E(n-r)$ from the color difference at $t=2$ days and fit a Cardelli et al. (1989) extinction curve with free R_V and A_V. In Figure 7, we show both the colors of SN 2020fqv (filled plus signs) and the best-fit extinction curve applied to the

[19] Our sample does not include other extinguished SNe, since we require a blue color to trigger UVOT. In the case of SN 2020fqv, UVOT was triggered by another group and thus had early UV and is included in this study.

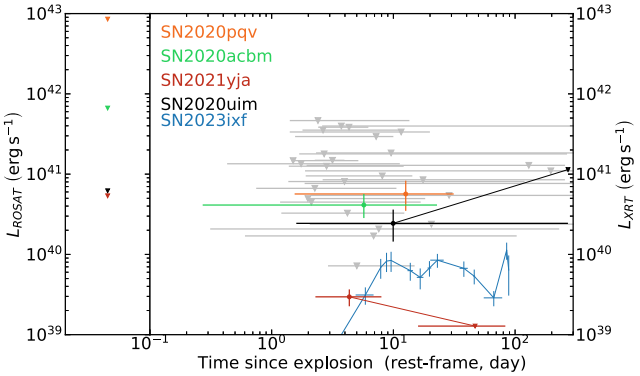

Figure 5. The right panel shows the XRT binned detections and upper limits for the SNe in our sample. Measurements were binned over the duration of the Swift observations, and the time of detections and upper limits is set to the mean photon arrival time. The left panel shows upper limits on the emission for the SN location for the four XRT detections from archival ROSAT survey data. We also show the XRT light curve of the nearby Type II SN 2023ixf (Zimmerman et al. 2024).

average SED (red points), which match well at both times. Here and in the rest of the paper, we assign wavelengths to filters using the pivot wavelength for a flat spectrum $\lambda_{\rm piv} = \sqrt{\frac{\int T(\lambda)\lambda d\lambda}{\int T(\lambda)\frac{d\lambda}{\lambda}}}$, where T is the filter transmission curve, downloaded from the Spanish Virtual Observatory (Rodrigo et al. 2012; Rodrigo & Solano 2020).[20]

In Figure 8, we show the calculated $E(n-r)$ for SN 2020fqv along with the best-fitting extinction curves. The computed posterior probability distribution in the $A_V - R_V$ plane is shown in the inset. Using our results, we can determine extinction to $E(B-V) = 0.1$ mag, on average, and with a maximum systematic uncertainty of $E(B-V) = 0.2$ mag. The case of SN 2020fqv demonstrates that for highly extinguished SNe, a tight constraint can be acquired on R_V. As UVM2 measurements for SN 2020fqv were not acquired, we cannot discriminate between extinction curves with and without the 220 nm feature. However, these can likely be distinguished if such measurements are available. For mildly extinguished SNe, one may limit the extinction using these data. In Table 5, we report the color for $t = 1$ to $t = 5$ days. When using this method to measure the extinction, we caution against using a single epoch to estimate the extinction, as it can be degenerate with a temperature difference from the SN II population.

We next consider intrinsic deviations from the blackbody. In Figure 9, we show color–color plots of the SNe in our sample at the first UV epoch. In panel (a), we plot the $W2-r$ and $g-r$ colors, and in panel (b), we plot the UVW2 − UVM2 and $g-r$ colors. Data points indicate the colors of the SNe II at their first UVOT visit, where blue and red colors represent SNe with and without flash features in their early spectra, respectively. The solid black line corresponds to a blackbody with zero extinction between 10,000 K and 100,000 K. The green contours show the expected color–color values of the models of M24 at $t = 1.5$–2.5 days for a range of model parameters. The effect of adding extinction with $E(B-V) = 0.2$ mag different R_V values is illustrated using green arrows.

The positions that various SNe occupy in Figure 9 demonstrate a clear deviation from a nonextinguished blackbody (black curve). SNe with and without flash features occupy the same area in the parameter space, indicating that this deviation from the blackbody is not related to the presence of optically thin CSM. Pure reddening can explain some of the deviation but requires $R_V > 3.1$, a high temperature close to 100,000 K, and an $E(B-V)$ of up to 0.4 mag for some of the objects—more than the 0.2 mag that we infer based on the scatter in the color curves. Relative to the expected color–color values predicted from the envelope-cooling models of M24, an extinction law with $R_V \geqslant 3.1$ is required to explain the position of all points. While other effects could mimic the bluer UV-optical colors of some of the points, a difference in R_V seems a better explanation. It is consistent with the colors of the various SNe in both the $W2-r$ color, where the value of R_V has a large effect on the color, and the W2 − M2 color, which is relatively unaffected by the value of R_V. On the other hand, a deviation caused by a line, e.g., in the W2 band, would have a more significant effect on the W2 − M2 color.

In panels (c) and (d), we show the expected color–color values from the analytic shock-cooling models of M24 at $E(B-V) = 0$–0.4 mag, including time-dependent deviations from the blackbody. Colored points represent a subset of SNe from our sample and their evolution in their first week. The time-dependent nature of the color curves (evolving from blue to red) conclusively indicates that some of the deviation is intrinsic (i.e., due to evolving line blanketing and line emission). For many of the objects, the color evolution is similar to the expected color evolution in the shock-cooling models, and a combination of mild $E(B-V) < 0.2$ mag, intrinsic deviations from the blackbody, and in some cases $R_V > 3.1$, can fully explain all SN colors. We note that line blanketing alone cannot explain the observed deviations, since the UV-optical colors are bluer than the blackbody that fits the optical colors alone. The color evolution of SN 2020pni (blue circles) stands out in our sample. Its $g-r$ color becomes bluer in the first few days of its evolution. Terreran et al. (2022) argue the early light curve of this SN is powered by a shock breakout in an extended wind, rather than cooling of a shocked envelope. This nonmonotonic color evolution was also observed for SN 2018zd (Hiramatsu et al. 2021) and the nearby SN 2023ixf (Hiramatsu et al. 2023; Jacobson-Galán et al. 2023; Li et al. 2024; Zimmerman et al. 2024), also suspected as a wind breakout.

To conclude, 33 of 34 SNe in our sample show $UVW2-r$ colors that become redder with time, consistent with a cooling behavior. Using the mean colors, the extinction of any SNe can be constrained to better than $E(B-V) = 0.2$ mag. The early UV-optical colors of SNe II indicate deviations from the blackbody that are consistent with the expected deviations due to extinction and the expected intrinsic deviations from the blackbody in a cooling envelope, with no additional CSM interaction required.

4.2. Blackbody Evolution

We linearly interpolate the UV-optical light curves of the sample SNe to the times of UV observations and construct an SED. Using the `Scipy curve_fit` package (Virtanen et al. 2020), we fit this SED to a Planck function and recover the

[20] We estimate that the $\lambda_{\rm piv}$ of a blackbody with $10{,}000 > T > 30{,}000$ (relevant to this study) will be within 5% of the $\lambda_{\rm piv}$ assuming a flat spectrum for all filters used in our study. While the flux conversion factors depend on the spectral shape (e.g., Brown et al. 2016), we estimate this effect to be less than 10% for a blackbody within this temperature range.

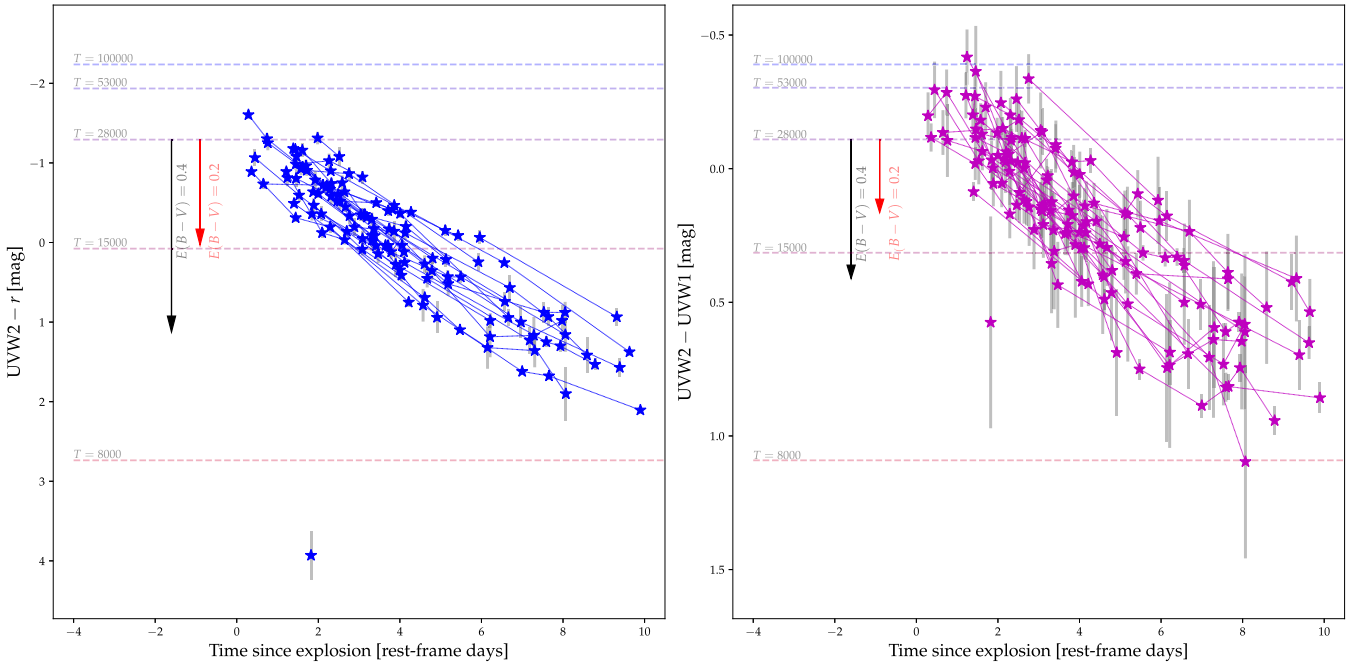

Figure 6. The color evolution of SNe II in our sample in the UVW2 − r (left panel) and UVW2 – UVW1 (right panel) bands. Each curve represents a single SN. The dashed lines are the colors of blackbodies at various temperatures. The arrows show the color difference due to extinction with $E(B-V)=0.2$ mag (red arrow) and $E(B-V)=0.4$ mag (black arrow), assuming a Milky Way extinction curve with $R_V=3.1$. The outlier in the left plot is the highly extinguished SN 2020fqv.

evolution of the blackbody temperature, radius, and luminosity parameters $T_{\rm eff}$, $R_{\rm BB}$, and $L_{\rm BB}$, respectively. We assume a 0.1 mag systematic error in addition to the statistical errors to account for imperfect cross-instrument calibration. In addition to the best-fit blackbody luminosity, we calculate a pseudobolometric luminosity by performing a trapezoidal integration of the interpolated SED and extrapolating it to the UV and infrared (IR) using the blackbody parameters. The fit results are reported in Table 3.

In Figure 10, we show the blackbody evolution for our sample SNe, as well as the mean blackbody evolution of the population. To do so, we interpolate the temperatures, radii, and luminosities with 0.5 day intervals and take the population mean separately for SNe with and without flash ionization features as determined by Bruch et al. (2021, 2023). We estimate the error on the population mean through a bootstrap analysis (Efron & Tibshirani 1993). We draw 34 SNe, allowing for repetitions. We then draw samples from the blackbody parameters of each SN assuming a Gaussian distribution for every fit point. We then interpolate to the same time grid and calculate the population mean at every time step. The blue histogram shows the fraction of SNe in our sample with blackbody fits as a function of time.

We find that SNe with flash features have a blackbody temperature $6.3\% \pm 4.1\%$ cooler and a radius (or photospheric velocity) $28\% \pm 11\%$ larger than SNe without flash features. This difference is highlighted in Figure 11, where we show the radius and temperature distribution of SNe with and without flash features interpolated to $t=2$ days after explosion. At all times where a significant >50% fraction of the sample has measurements, the mean blackbody properties are well described by the predictions of spherical phase shock cooling (fit to the population mean evolution). Our results indicate that the population of SNe II is well described by a cooling blackbody following shock breakout at the edge of a shell of material with a steep density profile.

4.3. Shock-cooling Fitting

4.3.1. Method and Validation

As the population blackbody evolution is well described by shock cooling, we fit individual SN light curves to shock-cooling models. We do this using the model presented in M23 and M24, which interpolates between the planar phase (i.e., when $r \approx R_{\rm bo}$) and the spherical phase (i.e., when $vt \gtrsim R_{\rm bo}$) of shock cooling and predicts the deviations of the SED from the blackbody as a function of model parameters. The full model is described in M23 and M24 and is briefly summarized in Section A.1.

The model has four independent physical parameters: the progenitor radius $R = R_{13}\, 10^{13}$ cm, the shock velocity parameter $v_{s*} = v_{s*,8.5}\, 10^{8.5}$ cm s^{-1}, the product of the density numeric scale factor f_ρ and the progenitor mass $M_* = M\, M_\odot$ (treated as a single parameter), and the envelope mass $M_{\rm env} = M_{\rm env,\odot}\, M_\odot$. In addition to these parameters, we also fit for the extinction curve, parameterized as a Cardelli et al. (1989) law with free R_V and $E(B-V)$, and the breakout time t_0.

As demonstrated in Rubin et al. (2016), adopting a fixed validity domain will create a bias against some large-radius models. For every model realization, we calculate the validity domain, omitting the points outside this validity range from consideration. In order to properly compare between models with a different number of valid points, we adopt a likelihood function based on the χ^2 probability density function (pdf), as described in detail in Soumagnac et al. (2020).

Shock-cooling models are expected to have residuals in temperature of order 5%–10% from model predictions (Rabinak & Waxman 2011; Sapir & Waxman 2017) when an average opacity is assumed and additional systematics due to the presence of lines. M24 expect the residuals on the flux to be of order 20%–40%, which will be correlated in time and wavelength. These residuals determine the appropriate

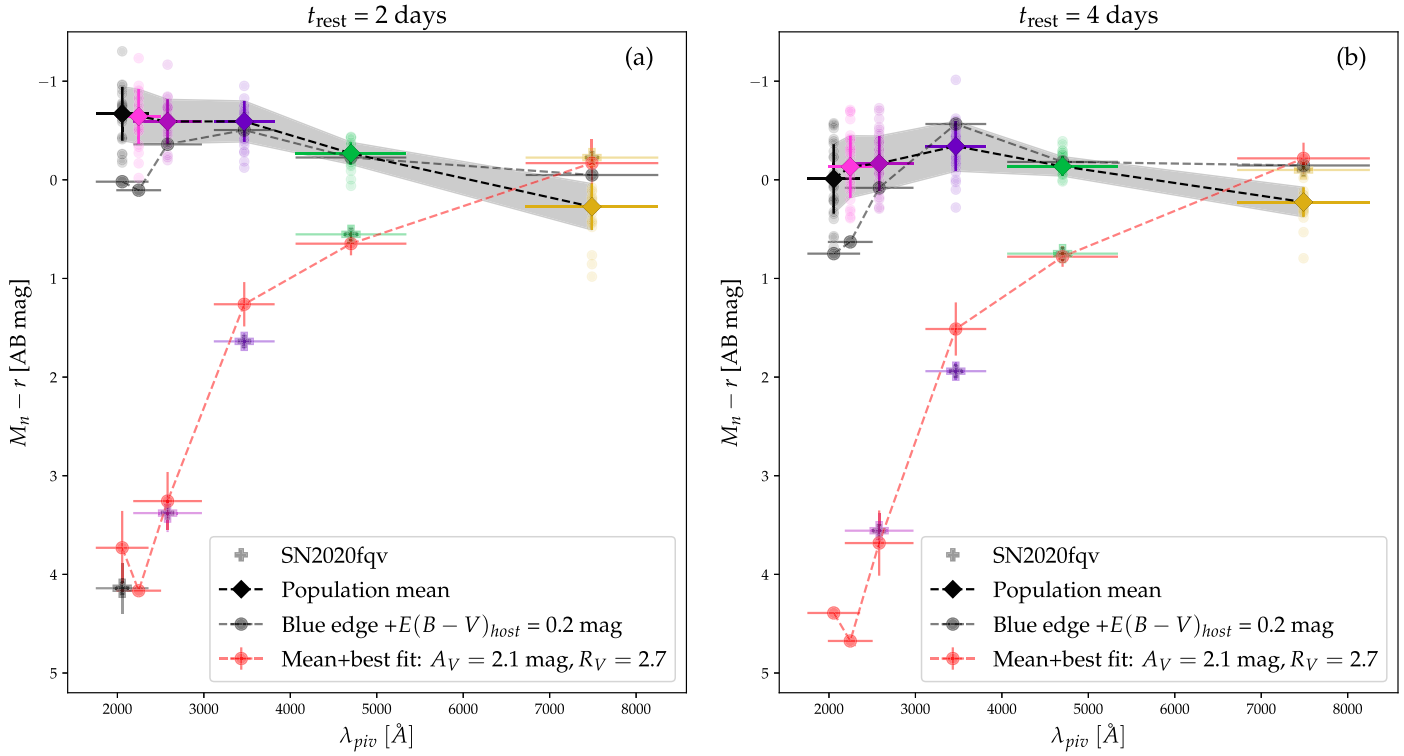

Figure 7. The mean colors of a sample of SNe II at (a) $t = 2$ days and (b) $t = 4$ days. The filled points and gray shaded regions show the mean color and the scatter of each color. The transparent points are individual SN colors. Both the mean and individual SN colors are color-coded by wavelength. The gray points demonstrate the effect of applying $E(B-V) = 0.2$ mag with an $R_V = 3.1$ Cardelli et al. (1989) extinction law to the bluest colors, demonstrating that the extinction in our sample is smaller than this value. The filled plus signs are the colors of the highly reddened SN 2020fqv. The red curve shows the effect of reddening the mean colors using the best-fit extinction curve, which reproduces the colors of SN 2020fqv to within the error bars for all wavelengths.

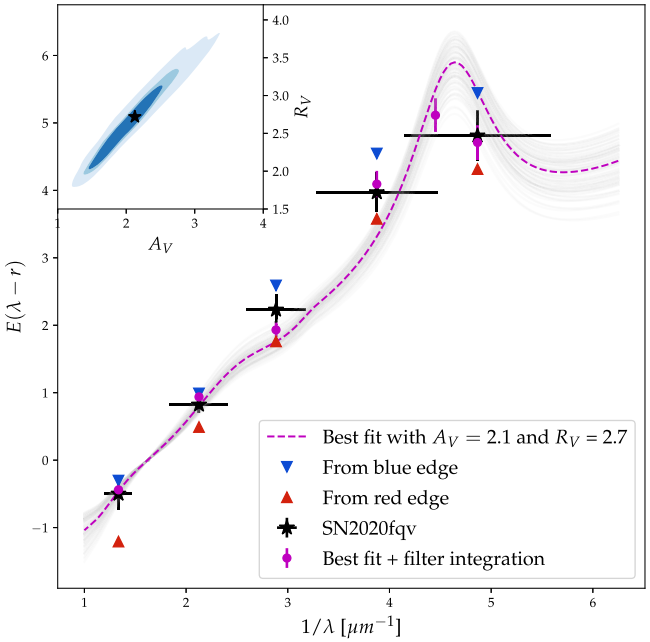

Figure 8. The best-fit extinction curve we find for SN 2020fqv by correcting it to the mean colors of SNe II. In each band, the downward- (upward-) pointing blue (red) triangle shows the limits of the value of A_λ from the bluest (reddest) objects in the sample. The black points show the color difference from the sample. The purple points are the best-fit extinction curve, applied on a spectrum of a blackbody with $T = 20{,}000$ K and integrated over the filter bandpass. The purple curve is the best-fit extinction law, and the gray transparent curves are 50 randomly drawn curves from the posterior distribution. In the inset, we show the posterior distribution of our fit, with colors indicating the 50%, 68%, and 95% confidence regions.

covariance matrix to use in the χ^2 statistic. They will also provide a criterion through which we can reject fits to a given data set. Indeed, when comparing the light curves of our sample of hydrodynamical simulations to the analytical model predictions, we find that 50% of the data points have residuals extending to 0.17 mag and 95% have residuals extending to 0.45 mag. To incorporate the correlation between residuals into our analysis, we construct a likelihood function using the following steps.

1. Given a set of light curves, we construct a set of synthetic measurements from the set of hydrodynamical simulations of M24 at the same times and photometric bands by integrating the simulated SED with the appropriate transmission filters.
2. From each simulation, we construct a set of residuals from the analytic model predicted by the physical parameters of each simulation.
3. For each light-curve point, we calculate the covariance term as the mean over all simulations, taking into account only simulations that are valid at that time.
4. Since the covariance matrix has too many parameters to be accurately estimated in full, we take the singular value decomposition of the mean covariance and keep the top three eigenvalues.[21] We then add this covariance matrix with a diagonal covariance matrix constructed from the observational errors in each data point and add a 0.1 mag systematic error for cross-instrument calibration.

[21] This choice accounts for >80% of the variance while preventing negative eigenvalues for any sampling used in our work.

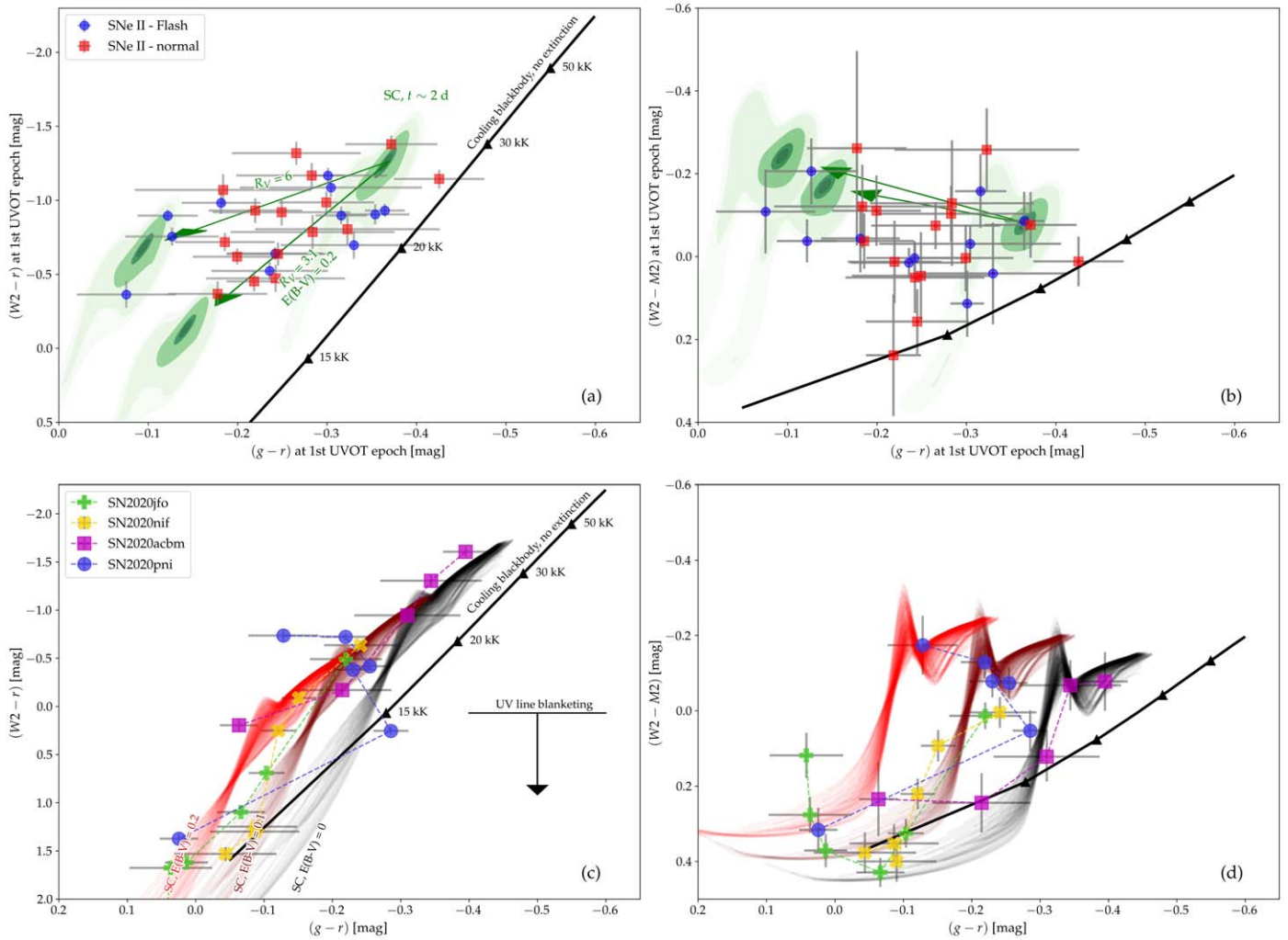

Figure 9. (a) Color–color diagram of the UVW2 – r and the optical $g - r$ color. The data points represent different SNe at their first UV epoch with (blue circles) and without (red squares) flash features. The solid black curve represents the colors of a blackbody with temperatures between 100 kK and 5 kK. The green contours show the expected color–color values of the models of M24 at $t = 1.5$–2.5 days for a range of model parameters. The effect of adding extinction with $E(B - V) = 0.2$ mag different R_V values is illustrated using green arrows. (b) is similar to (a), but for UVW2 − UVM2. (c) and (d) are similar to (a) and (b), but showing the color evolution of four SNe before $t < 7$ days. We also show model shock-cooling curves using the models of M24 with increasing $E(B - V)$ (0, 0.1, and 0.2 mag) using a Milky Way extinction law with $R_V = 3.1$. The distance from the black line corresponds to the deviation from the blackbody, which is present in all SNe studied in this work. For clarity and due to its red color, SN 2020fqv is not shown in this plot.

5. The likelihood of a model given the data is taken to be $\mathcal{L} = \mathrm{PDF}(\chi^2, \nu)$ where $\chi^2 = (d_i - m_i)\mathrm{cov}_{ij}^{-1}(d_j - m_j)$, where $\boldsymbol{d}$ and $\boldsymbol{m}$ are the data and the model, respectively; ν is the number of points where the model is valid; and the pdf is the χ^2 distribution pdf.

Using this likelihood, we fit the model to the photometry using the nested-sampling (Skilling 2006) package `dynesty` (Higson et al. 2019; Speagle 2020). We validate our method by testing that even in the presence of such residuals, we can still recover the true model parameters from simulated data sets. We fit all simulated data sets using this method and compare the fit parameters with the physical parameters used in the simulations. In Figure 12, we show an example of such a fit for a simulation generated with $R_{13} = 0.3$, $v_{s*,8.5} = 1.33$, and $M_{\rm env} = 1\,M_\odot$ with $E(B - V) = 0.1$ mag extinction added. We recover $R_{13} = 0.3 \pm 0.05$, $v_{s*,8.5} = 0.9 \pm 0.13$, $M_{\rm env} = 16 \pm 7.8\,M_\odot$, and $E(B - V) = 0.04 \pm 0.03$ mag.

In Figure 13, we show the fit and true radii R_{13} and shock velocity parameter $v_{s*,8.5}$ compared to the parameters used in the simulations. The 90% confidence intervals for parameter recovery are 30% for R_{13}, 26% for $v_{s*,8.5}$, and better than 0.05 mag in $E(B - V)$ over the entire parameter space of our simulations. However, we cannot recover $M_{\rm env}$ or $f_\rho M_{\rm tot}$ to better than an order of magnitude, and our fit results are highly sensitive to our choice of prior in those parameters, indicating they cannot be effectively constrained from shock-cooling modeling.

Our results demonstrate that even given significant residuals, one may still fit these analytic models and recover the shock velocity, progenitor radius, and amount of dust reddening with no significant biases. Our results also demonstrate that rejecting shock cooling as the main powering mechanism of the early light curves requires residuals larger than ∼0.5 mag.

4.3.2. Light-curve Fits

We ran our fitting routine on all sample SNe. We used log-uniform priors for $R_{13} \in [0.1, 30]$, $v_{s*,8.5} \in [0.1, 6]$, $f_\rho M \in [0.1, 200]$, and $M_{\rm env,\odot} \in [0.3, 30]$. We also fit $t_{\rm exp} \in [t_{\rm ND} - 1, t_{\rm first}]$ with a uniform prior, where $t_{\rm ND}$ is the last nondetection and $t_{\rm first}$

Table 3
Early-time Blackbody Fits of SNe Included in This Work (Truncated)

SN	t (rest-frame days)	$T_{\rm eff}$ (K)	$R_{\rm BB}$ (10^{14} cm)	$L_{\rm pseudo}$ (10^{42}erg s^{-1})	$L_{\rm pseudo,extrap}$ (10^{42}erg s^{-1})	χ^2/dof
SN 2018cxn	1.6	23,500 ± 1500	2.15 ± 0.16	3.749 ± 0.009	10.0 ± 0.7	1.4
SN 2018cxn	2.19	20,800 ± 1400	2.58 ± 0.22	3.767 ± 0.009	8.7 ± 0.5	2.2
SN 2018cxn	5.6	12,700 ± 600	5.3 ± 0.42	3.497 ± 0.007	5.1 ± 0.1	2.0
SN 2018cxn	9.59	10,500 ± 300	6.82 ± 0.34	2.827 ± 0.007	3.88 ± 0.04	0.6
SN 2018dfc	1.58	22,000 ± 800	4.31 ± 0.2	13.18 ± 0.02	31.0 ± 1.0	1.0
SN 2018dfc	3.19	17,000 ± 500	5.99 ± 0.25	12.46 ± 0.02	21.7 ± 0.4	1.0
SN 2018dfc	4.1	15,000 ± 300	6.92 ± 0.21	10.69 ± 0.02	17.1 ± 0.2	0.5
SN 2018dfc	5.03	13,300 ± 200	8.19 ± 0.29	9.88 ± 0.02	14.7 ± 0.1	0.5
SN 2018fif	1.22	20,600 ± 1500	1.68 ± 0.14	1.671 ± 0.003	3.7 ± 0.3	2.7
SN 2018fif	1.25	20,100 ± 1100	1.73 ± 0.12	1.646 ± 0.003	3.5 ± 0.2	2.1
SN 2018fif	2.1	15,600 ± 500	2.7 ± 0.15	1.851 ± 0.003	3.08 ± 0.06	1.6
SN 2018fif	2.65	15,100 ± 700	2.87 ± 0.21	1.813 ± 0.003	2.96 ± 0.07	2.9
SN 2018fif	4.57	12,000 ± 600	4.22 ± 0.3	1.976 ± 0.003	2.65 ± 0.05	3.6
SN 2018fif	6.15	11,200 ± 600	4.86 ± 0.42	2.041 ± 0.003	2.68 ± 0.05	4.4
SN 2018fif	6.17	11,100 ± 600	4.87 ± 0.42	2.042 ± 0.003	2.68 ± 0.05	4.4
SN 2018fif	7.31	10,600 ± 600	5.33 ± 0.46	2.037 ± 0.003	2.66 ± 0.04	4.2
SN 2018fif	8.33	10,000 ± 500	5.86 ± 0.49	1.997 ± 0.004	2.6 ± 0.04	3.5

Notes. A 0.1 mag systematic error was adopted for the fitting.

(This table is available in its entirety in machine-readable form in the online article.)

is the first detection, respectively (relaxing the prior on $t_{\rm ND}$ does not significantly impact our fit). Motivated by our analysis in Section 4.1, we also fit for host-galaxy extinction by assuming a Cardelli et al. (1989) reddening law with uniform priors on $E(B-V)$ and R_V in the range $E(B-V)\in[0,\ 0.25]$ mag and $R_V\in[2,\ 5]$. For SN 2020fqv, we fit with a wide prior of $E(B-V)\in[0.25,\ 1]$ mag, given the high host extinction we inferred from its color evolution.

In addition to the flat priors on the parameters, we include nonrectangular priors through the model validity domain. This is done to prevent fits that exclude most data points from the validity range for parameter combinations with high $v_{s*,8.5}$ and low $M_{\rm env}$. We assign zero probability to models that have no photometry data within their validity domain. While this does not impact our results in this work, fitting models without good nondetection limits shortly before explosion or that are expected to have short validity times (e.g., due to small radii or high velocity-to-envelope mass ratios) might be affected by this demand. In Soumagnac et al. (2020), we assigned priors on the recombination time at $0.7\,{\rm eV}=8120$ K ($t_{0.7\ {\rm eV}}\sim R_{13}^{0.56}v_{s*,8.5}^{0.16}$) of the SN through it spectral sequence. However, in some of the simulations of M24, we start seeing signs of hydrogen emission already at 20,000 K. Instead, we use priors derived from the blackbody sequence of the SN. Since there are residuals in color between the simulations and models, and since the effect of host-galaxy extinction is known to better than 0.2 mag, the fit temperature assuming $E(B-V)=0$ mag might not always be accurately used to determine the true photospheric temperature. We quantify the maximal effect of these systematics on the photospheric temperature near $0.7\,{\rm eV}=8120$ K. We fit all synthetic data sets (with an extinction of up to $E(B-V)=0.2$ mag) with blackbody SEDs assuming no host extinction and find that demanding $T>10{,}700$ K is enough to determine that $t>t_{0.7{\rm eV}}$, and $T<5500$ is enough to determine that $t<t_{0.7{\rm eV}}$ for any combination of parameters, as long as $E(B-V)\leqslant 0.2$ mag. These physically motivated priors on the recombination time have a significant effect on our fitting process.

Due to the peculiar temperature and luminosity evolution of SN 2020pni, which does not fit the general predictions of spherical phase shock cooling, we omit this SN from the fitting process. We will treat the modeling of this SN in detail in E. Zimmerman et al. (2024, in preparation).

In Table 4, we report the parameters of our posterior sampling at the 10th, 50th, and 90th percentiles. In all cases, we find good fits for the light curves at $t>1$ day after explosion. Our fits are divided into two cases. (1) For 15 SNe, we find good fits to the UV-optical SN light curves throughout the evolution. These models are characterized by a radius under 10^{14} cm and residuals better than 0.42 mag (95%) throughout the first week. (2) For the remaining 18 SNe, the early optical light-curve points do not match the rise of the models—either pushing them out of the model validity domain or missing them completely by more than 1 mag. These models are exclusively characterized by the large radius ($>10^{14}$ cm) required to account for a high luminosity but do not show the shallow rise or double-peaked feature expected for planar phase shock cooling of such a star.[22] After the first day from estimated explosion, these fits have comparable residuals to group 1. If forced to fit a radius of $<10^{14}$ cm, a reasonable fit is achieved in about half of the cases. For the rest of the objects in this group, forcing a small radius results in a bad overall fit.

Since the spherical phase luminosity $L_{\rm RW}\sim R_{13}v_{s*,8.5}^{1.91}$, these fits are characterized by a higher $v_{s*,8.5}$ and more host-galaxy extinction to decrease the temperature as $T_{\rm ph,t=1\ d}\sim R_{13}^{1/4}v_{s*,8.5}^{0.07}$. We show examples of fits of both cases in Figure 14 and make all figures of all light-curve fits available. In Figure 15, we show the illuminating example of SN 2020nvm, which was observed by TESS throughout its rise. We show that a model accounting only for the spherical phase will artificially create a much sharper rise compared to a model that fits the peak. In this case, our best small-radius fit did not match the observed light curve well, and the large-radius model (one of the largest

[22] In the Rayleigh–Jeans limit, this can be intuitively understood as $f_\lambda\propto T_{BB}R_{BB}^2$, resulting in $f_\lambda\propto t^{-1/3}$ in the planar phase, and $f_\lambda\propto t^{1.15}$ early in the spherical phase.

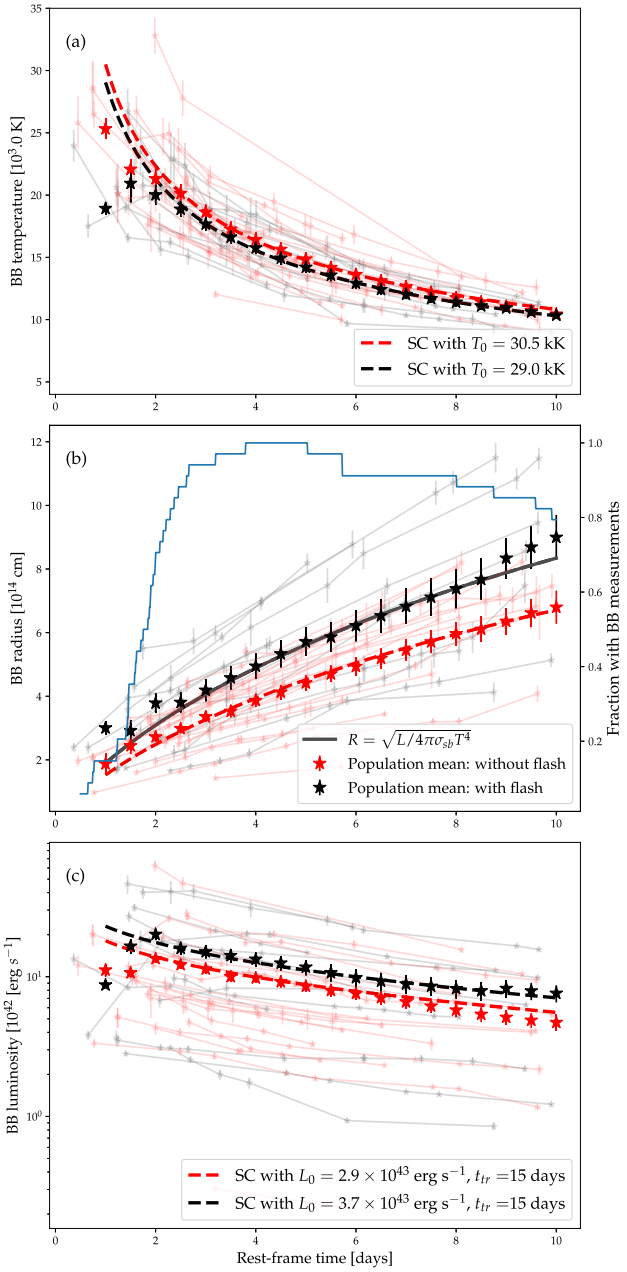

Figure 10. The blackbody evolution of a sample of SNe II during the first 10 days. The transparent points represent individual SNe, color-coded according to the presence of flash features (black) or lack thereof (red). The blue curve indicates the fraction of the sample with blackbody fits at each time step. The filled points show the population mean, and the dashed curves show the predicted evolution according to spherical phase shock cooling. Panels (a)–(c) show the blackbody temperature, radius, and luminosity, respectively. The match between the predictions of spherical phase shock-cooling models and the population blackbody evolution motivates the use of these models to fit individual SN light curves.

values in our sample) misses the rise. The clear first peak expected in planar phase cooling is not observed even at early times.[23] The Sapir & Waxman (2017) model fits the rise much better, although it is not physical at early times.

[23] We note that some features are present in the very early light curve. These are also present in some of the simulations of M24 and could be the result of lines. This is likely not the shock-breakout signal, which is expected to be very faint in this band (Katz et al. 2013; Sapir et al. 2013; Sapir & Halbertal 2014).

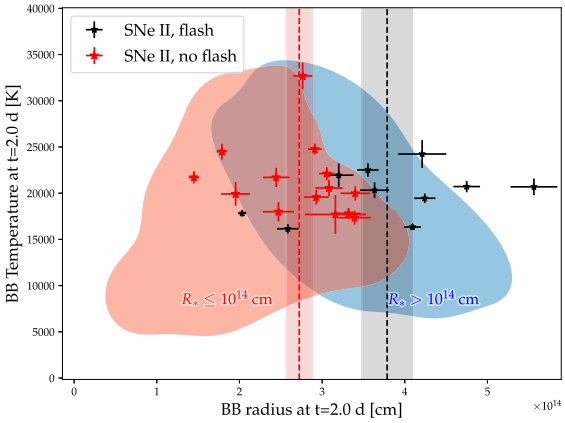

Figure 11. The distribution of blackbody temperature and radius, interpolated to $t = 2$ days. Black and red points are SNe II with and without flash features, respectively. The dashed lines and shaded regions show the population mean and standard error. The red and blue colored regions show the area occupied by simulated progenitors with $<10^{14}$ cm and $>10^{14}$ cm, respectively. These are generated by fitting a blackbody to synthetic data sets constructed from the multigroup simulations of M24. Of the 23 SNe with a measurement at this time, seven are only consistent with simulations that have a breakout radius $>10^{14}$ cm or a shock velocity parameter $v_{s*} \gtrsim 6000$ km s^{-1}.

In Figure 16, we present the posterior probability for the radius of best-fit models that miss the rise and those that match the rise. We find no statistically significant difference between SNe with and without flash features (which could perhaps be detected given a larger sample).

We summarize the different categories our objects fall into in Figure 17. Most SNe II are cooling at early times, showing constant or reddening UV-optical colors. We refer to these as "II-C." SNe II that are heating and showing a bluer UV-optical color with time are referred to as "II-H." We further subdivide the II-C group into SNe with a small fit radius ("II-C+"), which are well fit at early times, and those with a large fit radius ("II-C-"), which are not well fit by shock-cooling models at early times.

5. Discussion

5.1. RSG Radius Distribution

5.1.1. What Can the Early-time Fits Teach Us?

In Section 4.3.1, we demonstrated that with a typical set of UV-optical light curves, we can recover the breakout radius and shock velocity parameter from the simulations of M24 for a wide range of parameters. When applying our method to the SNe of our sample, we found good fits to roughly half of the SNe, with radii consistent with the observed RSG radius distribution (II-C+). The remaining SNe systematically miss the rise and are characterized by either a high R_{13} or a high $v_{s*,8.5}$ due to the higher luminosity of this group compared to other SNe (II-C-). Since there are acceptable fits for roughly half of such SNe, and as the blackbody radius and temperatures of the majority of the sample evolve according to the predictions of spherical phase shock cooling, we cannot rule out that it is the primary powering mechanism of these SNe. Our lack of early-time UV-optical colors and of high-quality sampling in the first hours of the SN explosions prevents us from testing whether the blackbody evolution in the very early times evolves according to the predictions of planar phase shock cooling. However, we note that when optical colors are

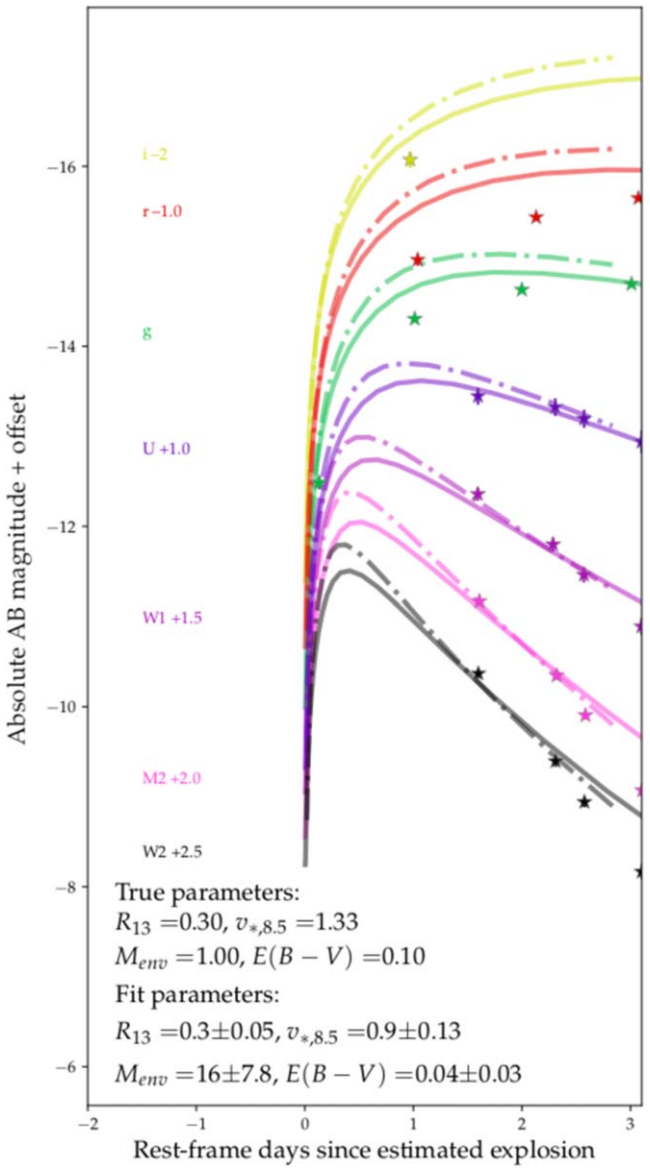

Figure 12. Example of shock-cooling fits to a multiband synthetic data set, compared to the models generated from the physical simulation parameters. The solid lines are the average fits from the posterior, and the dotted–dashed lines are model generated from the physical simulation parameters. The model light curves typically deviate by up to 20% (calibration uncertainty) from the simulations and are expected to deviate by up to 40% in band-specific flux due to theoretical uncertainty. We show the model until its upper validity time. The best-fit model accurately reproduces the breakout radius and velocity and finds a similar $E(B-V)$ but cannot reproduce the envelope mass or other model parameters.

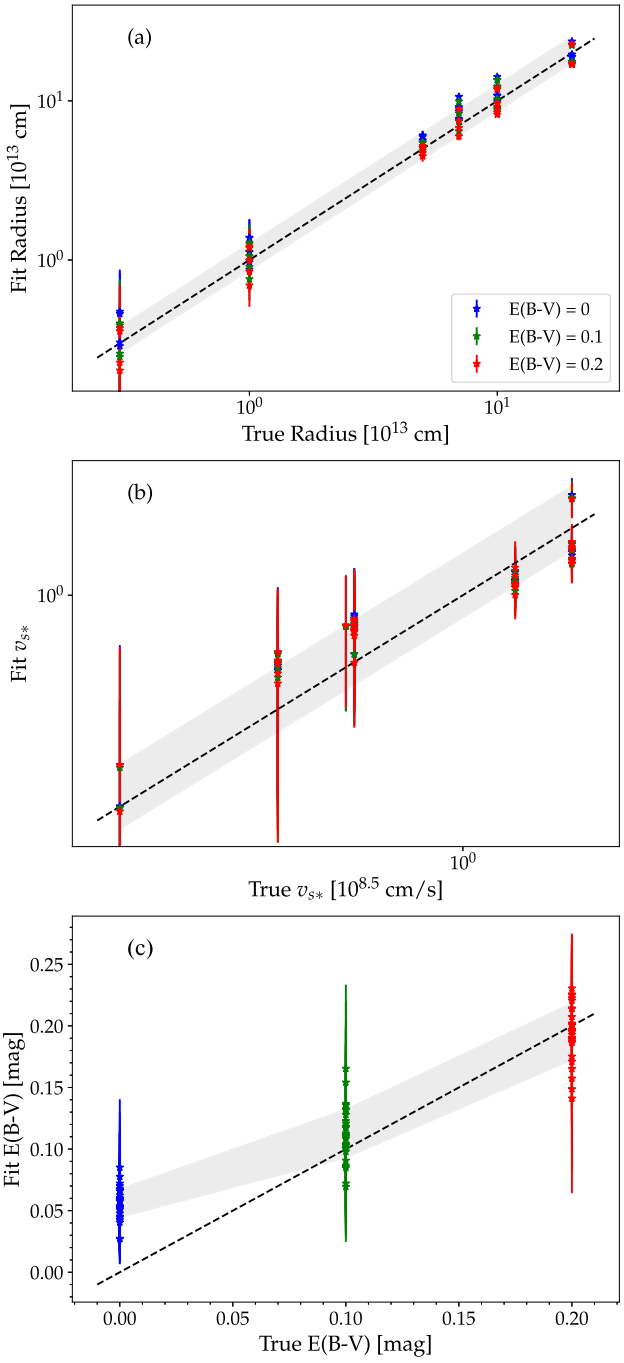

Figure 13. Parameter recovery when fitting a sample of synthetic light curves with analytic shock-cooling models. In panels (a) and (b), we show the fit and true parameters for R_{13} and $v_{s*,8.5}$, respectively. In panel (c), we show the recovery accuracy of $E(B-V)$. The dashed line represents a perfect recovery, and the shaded regions represent the 68% interval over the full parameter space.

available during these first phases, the colors are consistent with that of a hot >15,000 K blackbody. With this in mind, there are several possibilities to explain the large-radius fits.

1. These SNe are powered by shock cooling only and have a small radius. The failure to fit the rise is due to correlated residuals not present in the simulations and thus is not modeled in the covariance matrix we used, creating a bias to larger radii in some cases, or they did not cover this particular combination of shock velocity and radius. This possibility is likely what happens in half of the cases, where a good fit is acquired if the fit is forced to a small radius. In other cases, the small-radius fit still misses the rise, or a unrealistically high v_{s*} is required.
2. These SNe have a large progenitor radius, and their early-time evolution does not fit the predictions of planar phase shock cooling from a spherical RSG envelope. Recent work by Goldberg et al. (2022a, 2022b) shows that the turbulent 3D structure of the outer regions of the envelope or a nonspherical breakout surface could possibly extend the duration of shock breakout and affect the early stages of shock cooling up to a timescale of

Table 4
Best-fit Parameters for Shock-cooling Fitting

SN	R_{13}^{b}	$v_{s*,8.5}^{b}$	$f_{M^{b}}$	$E(B-V)^{b}$ (mag)	R_V^{b}	$t_0^{a,b}$ (JD)	$t_{0.7}^{a,b}$ (days)	$t_{tr}^{a,b}$ (days)
SN2018cxn	$9.8^{+4.2}_{-4.8}$	$1.7^{+0.7}_{-0.5}$	$12.0^{+21.7}_{-11.8}$	$0.07^{+0.04}_{-0.04}$	$3.8^{+1.0}_{-1.2}$	$-0.01^{+0.08}_{-0.07}$	24.2	4.8
SN2018dfc	$24.3^{+4.2}_{-4.3}$	$3.4^{+0.5}_{-0.4}$	$0.7^{+0.7}_{-0.6}$	$0.10^{+0.03}_{-0.03}$	$3.4^{+1.1}_{-1.1}$	$-0.02^{+0.08}_{-0.06}$	52.3	3.0
SN2018fif	$8.9^{+4.1}_{-7.1}$	$1.1^{+0.8}_{-0.4}$	$67.7^{+88.6}_{-65.8}$	$0.14^{+0.05}_{-0.06}$	$3.2^{+1.0}_{-0.9}$	$0.03^{+0.05}_{-0.06}$	9.2	3.8
SN2019eoh	$5.9^{+2.0}_{-1.9}$	$2.9^{+0.9}_{-0.9}$	$20.7^{+46.9}_{-20.4}$	$0.04^{+0.04}_{-0.03}$	$3.6^{+1.1}_{-1.2}$	$-0.00^{+0.08}_{-0.08}$	29.3	3.0
SN2019gmh	$13.4^{+15.3}_{-11.6}$	$2.0^{+1.6}_{-1.5}$	$21.5^{+58.3}_{-21.3}$	$0.12^{+0.10}_{-0.10}$	$3.4^{+1.2}_{-1.2}$	$-0.22^{+0.29}_{-0.20}$	12.5	3.8
SN2019nvm	$20.4^{+6.9}_{-6.7}$	$1.8^{+0.6}_{-0.6}$	$11.9^{+22.5}_{-11.7}$	$0.16^{+0.05}_{-0.05}$	$3.7^{+1.0}_{-1.1}$	$-0.70^{+0.29}_{-0.23}$	39.9	4.3
SN2019omp	$18.0^{+6.5}_{-13.5}$	$1.6^{+1.1}_{-0.6}$	$21.3^{+46.9}_{-21.0}$	$0.17^{+0.04}_{-0.04}$	$3.0^{+0.9}_{-0.8}$	$-0.01^{+0.08}_{-0.07}$	33.2	6.5
SN2019oxn	$6.7^{+2.4}_{-2.3}$	$0.7^{+0.3}_{-0.2}$	$7.5^{+11.2}_{-7.1}$	$0.05^{+0.04}_{-0.04}$	$3.5^{+1.1}_{-1.1}$	$-0.03^{+0.12}_{-0.11}$	15.6	16.7
SN2019ozf	$20.3^{+4.7}_{-4.4}$	$1.6^{+0.5}_{-0.5}$	$13.7^{+27.7}_{-13.5}$	$0.14^{+0.04}_{-0.04}$	$3.5^{+1.1}_{-1.1}$	$-0.01^{+0.08}_{-0.07}$	47.9	5.0
SN2019ust	$5.3^{+3.3}_{-2.6}$	$3.3^{+1.4}_{-1.3}$	$11.4^{+20.3}_{-11.2}$	$0.16^{+0.05}_{-0.04}$	$3.3^{+1.1}_{-1.0}$	$0.06^{+0.12}_{-0.15}$	13.3	3.2
SN2019wzx	$7.0^{+8.2}_{-5.2}$	$3.3^{+1.5}_{-1.5}$	$23.6^{+56.9}_{-23.3}$	$0.08^{+0.08}_{-0.06}$	$3.3^{+1.2}_{-1.0}$	$-0.01^{+0.10}_{-0.10}$	28.4	3.5
SN2020aavm	$17.7^{+8.3}_{-8.7}$	$0.9^{+0.4}_{-0.3}$	$29.8^{+69.1}_{-29.5}$	$0.07^{+0.07}_{-0.06}$	$3.5^{+1.1}_{-1.1}$	$-0.18^{+0.58}_{-0.47}$	25.6	6.3
SN2020abue	$18.7^{+7.3}_{-11.6}$	$0.8^{+0.4}_{-0.4}$	$69.2^{+101.1}_{-68.2}$	$0.11^{+0.07}_{-0.10}$	$3.0^{+1.1}_{-0.8}$	$-0.02^{+0.13}_{-0.12}$	34.7	10.5
SN2020acbm	$16.8^{+2.2}_{-2.2}$	$1.2^{+0.6}_{-0.4}$	$53.1^{+97.1}_{-52.8}$	$0.06^{+0.03}_{-0.03}$	$3.4^{+1.1}_{-1.0}$	$-0.02^{+0.08}_{-0.06}$	23.8	8.2
SN2020afdi	$13.3^{+3.1}_{-3.0}$	$0.3^{+0.1}_{-0.1}$	$27.0^{+61.1}_{-26.7}$	$0.08^{+0.06}_{-0.06}$	$3.5^{+1.1}_{-1.1}$	$-0.05^{+0.26}_{-0.24}$	16.6	29.7
SN2020cxd	$5.4^{+2.7}_{-2.5}$	$0.3^{+0.1}_{-0.1}$	$30.1^{+68.3}_{-29.7}$	$0.11^{+0.09}_{-0.08}$	$3.4^{+1.2}_{-1.1}$	$-0.07^{+0.52}_{-0.48}$	8.9	10.1
SN2020dyu	$21.6^{+5.1}_{-5.2}$	$2.5^{+0.8}_{-1.0}$	$9.0^{+12.8}_{-8.9}$	$0.08^{+0.05}_{-0.05}$	$3.3^{+1.2}_{-1.0}$	$-0.01^{+0.08}_{-0.07}$	36.5	3.5
SN2020fqv	$2.0^{+1.8}_{-1.3}$	$1.9^{+1.1}_{-0.9}$	$21.1^{+49.5}_{-20.8}$	$0.75^{+0.14}_{-0.12}$	$2.7^{+0.6}_{-0.5}$	$-0.00^{+0.15}_{-0.14}$	12.1	6.1
SN2020jfo	$3.3^{+3.0}_{-2.5}$	$1.5^{+0.8}_{-0.7}$	$12.5^{+25.4}_{-12.3}$	$0.06^{+0.06}_{-0.05}$	$3.4^{+1.1}_{-1.1}$	$-0.20^{+0.21}_{-0.18}$	13.2	7.2
SN2020lfn	$18.5^{+6.0}_{-5.7}$	$3.1^{+0.9}_{-0.9}$	$15.2^{+31.3}_{-15.0}$	$0.04^{+0.03}_{-0.03}$	$3.5^{+1.1}_{-1.1}$	$-0.01^{+0.08}_{-0.07}$	38.4	3.9
SN2020mst	$21.1^{+5.8}_{-5.8}$	$1.6^{+0.6}_{-0.5}$	$22.8^{+54.2}_{-22.5}$	$0.12^{+0.04}_{-0.04}$	$3.4^{+1.1}_{-1.1}$	$0.00^{+0.09}_{-0.09}$	43.1	7.8
SN2020nif	$7.4^{+10.7}_{-4.9}$	$3.0^{+1.3}_{-1.1}$	$25.8^{+60.9}_{-25.5}$	$0.06^{+0.08}_{-0.05}$	$3.2^{+1.2}_{-1.0}$	$-0.50^{+0.26}_{-0.22}$	17.6	5.3
SN2020nyb	$12.5^{+4.7}_{-4.1}$	$0.7^{+0.3}_{-0.2}$	$41.0^{+81.7}_{-40.4}$	$0.11^{+0.09}_{-0.09}$	$3.3^{+1.1}_{-1.0}$	$-0.01^{+0.08}_{-0.07}$	16.7	14.2
SN2020pqv	$19.1^{+4.0}_{-3.8}$	$1.4^{+0.4}_{-0.4}$	$32.2^{+73.4}_{-31.7}$	$0.08^{+0.04}_{-0.04}$	$3.5^{+1.1}_{-1.1}$	$-0.01^{+0.08}_{-0.07}$	40.7	4.9
SN2020qvw	$10.6^{+12.3}_{-7.2}$	$3.4^{+1.2}_{-1.3}$	$8.2^{+12.2}_{-8.0}$	$0.05^{+0.04}_{-0.04}$	$3.3^{+1.2}_{-1.0}$	$-0.26^{+0.17}_{-0.14}$	11.8	3.2
SN2020ufx	$25.0^{+4.0}_{-4.6}$	$3.3^{+1.1}_{-0.9}$	$20.9^{+49.1}_{-20.7}$	$0.09^{+0.03}_{-0.03}$	$3.1^{+1.0}_{-0.9}$	$-0.01^{+0.08}_{-0.08}$	43.3	4.4
SN2020uim	$14.5^{+2.3}_{-2.3}$	$0.4^{+0.2}_{-0.1}$	$63.4^{+89.2}_{-59.8}$	$0.05^{+0.04}_{-0.04}$	$3.3^{+1.2}_{-1.0}$	$0.03^{+0.05}_{-0.05}$	20.8	34.6
SN2020xhs	$16.5^{+6.4}_{-5.7}$	$0.6^{+0.2}_{-0.2}$	$34.5^{+75.1}_{-34.1}$	$0.10^{+0.08}_{-0.07}$	$3.4^{+1.2}_{-1.1}$	$-0.04^{+0.26}_{-0.22}$	17.5	6.2
SN2020xva	$17.7^{+5.2}_{-5.0}$	$0.6^{+0.2}_{-0.2}$	$38.8^{+85.1}_{-38.5}$	$0.15^{+0.08}_{-0.09}$	$3.6^{+1.1}_{-1.1}$	$-0.04^{+0.55}_{-0.52}$	24.8	6.9
SN2021apg	$15.0^{+9.9}_{-9.8}$	$1.0^{+0.4}_{-0.4}$	$35.4^{+81.3}_{-35.1}$	$0.11^{+0.09}_{-0.09}$	$3.4^{+1.2}_{-1.1}$	$-0.03^{+0.17}_{-0.14}$	33.6	7.1
SN2021ibn	$20.4^{+7.1}_{-9.8}$	$2.1^{+1.0}_{-0.7}$	$17.0^{+36.1}_{-16.8}$	$0.03^{+0.03}_{-0.03}$	$3.5^{+1.1}_{-1.2}$	$0.12^{+0.17}_{-0.31}$	52.1	6.3
SN2021skn	$15.3^{+11.1}_{-12.7}$	$1.8^{+1.6}_{-0.9}$	$36.6^{+76.4}_{-36.0}$	$0.04^{+0.05}_{-0.04}$	$3.1^{+1.2}_{-0.9}$	$-0.49^{+0.31}_{-0.23}$	26.8	3.7
SN2021yja	$16.2^{+2.5}_{-2.5}$	$0.7^{+0.1}_{-0.1}$	$109.1^{+71.8}_{-71.0}$	$0.08^{+0.03}_{-0.03}$	$3.7^{+1.1}_{-1.2}$	$0.61^{+0.06}_{-0.06}$	23.0	6.4

Notes.
[a] All times are in rest-frame days.
[b] Uncertainties reflect the 10th–90th percentiles of the posterior probability distribution.

(This table is available in its entirety in machine-readable form in the online article.)

$R/v \lesssim 1$ day. If this is the case for the majority of similar fits, the large radius of the progenitor star would be consistent with a shell of dense CSM or an inflated envelope at $<3 \times 10^{14}$ cm, with the breakout occurring at the edge of the shell. This interpretation is also supported by spectropolarimetric observations of SN 2021yja (Vasylyev et al. 2024), showing a high degree of continuum polarization during the early photospheric phase ($t > 25$ days). SN 2021yja is well fit by a large-radius model during its full evolution but misses the rise by several magnitudes. The large-radius fit is also noted by Hosseinzadeh et al. (2022), who fit the spherical phase model of Sapir & Waxman (2017) and acquire very similar parameters, but their fit matches the rise at early times due to lacking an accurate description of the planar phase. A similar case is demonstrated in Figure 15.

3. These SNe are the result of a breakout from the edge of a shell of dense CSM on a several-hours timescale, and the early (few days) light curve is characterized by the subsequent cooling. The intrinsic timescale (i.e., ignoring light travel time) for shock breakout from any spherical density profile is $\frac{\Delta R}{v} = \frac{c}{v_{bo}^2 \kappa \rho_{bo}}$, where ΔR is the width of the breakout shell and v_{bo} and ρ_{bo} are the velocity and density at breakout (Waxman & Katz 2017, and references therein). A shock breakout in a slowly declining and extended density profile will be characterized by a density of $\lesssim 10^{-12}$ g cm^{-3} and occur on a timescale of a few days. This is likely what occurred during the explosions of SN 2020pni, SN 2018zd (Hiramatsu et al. 2021), and, more recently, SN 2023ixf (Zimmerman et al. 2024), where a rise in temperature was observed during the first few days. In both cases, breakout occurred from a shell of dense CSM confined to $<2 \times 10^{14}$ cm. If the mass of this shell is higher, breakout will occur at the edge of the shell at densities of

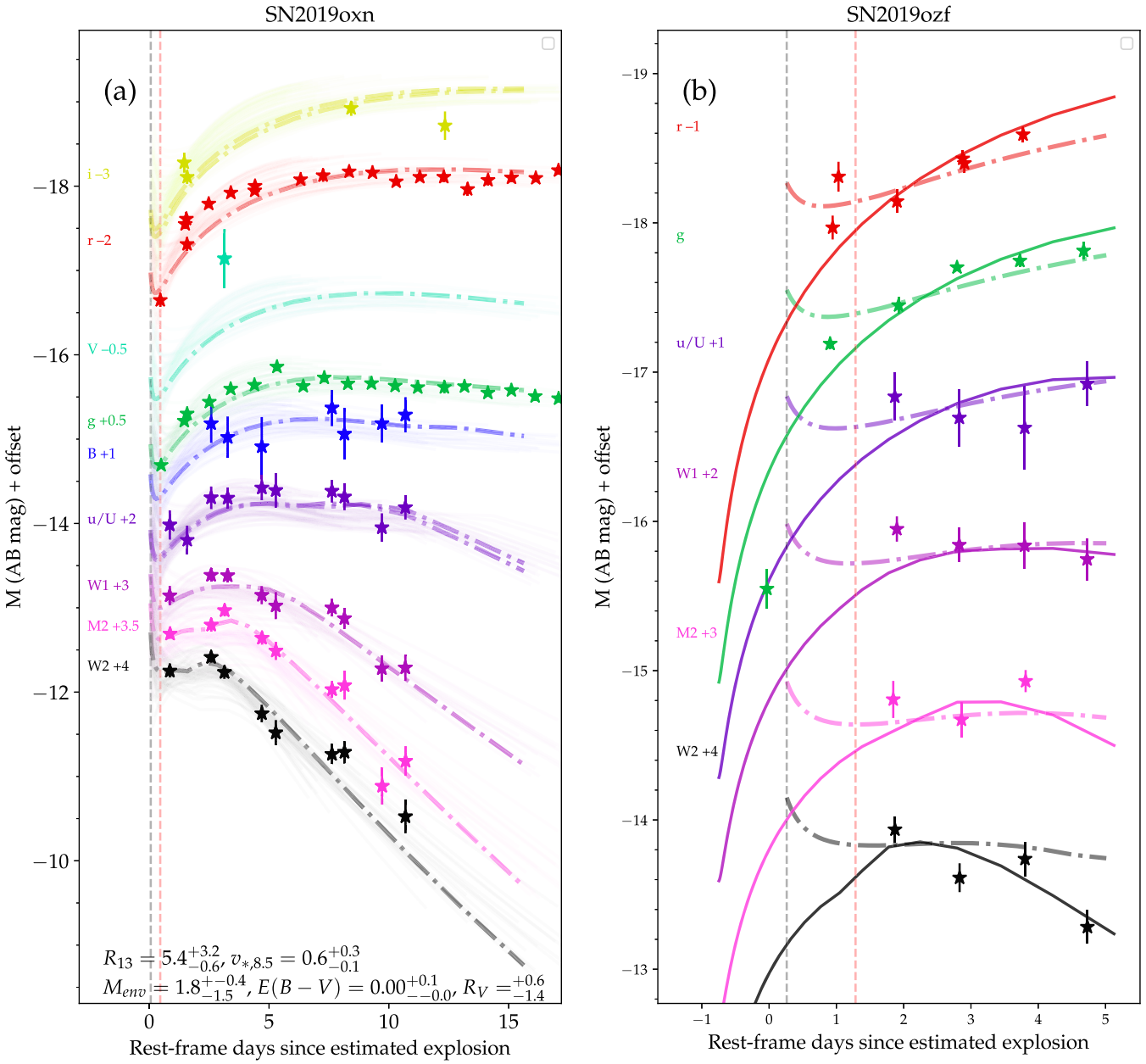

Figure 14. (a) An example of a fit to an SN data set from our sample. The dotted–dashed curves are the best fits in each band. The transparent curves are 50 random samples from the posterior distribution. The vertical dashed lines indicate the best-fit lower validity domain (gray) and the transition from planar to spherical phase (orange). (b) An example of a fit that misses the rise (the first g-band point) for the best-fit model ($R_{13} = 22.2$, $v_{s*,8.5} = 1.7$; dotted–dashed lines) but to which a reasonable lower radius fit exists ($R_{13} = 4.0$, $v_{s*,8.5} = 3.3$; solid lines).
(The complete figure set (33 images) is availablein the online article.)

$\rho_{\rm bo} \sim 10^{-11}$ g cm^{-3}, resulting in an hours-long breakout that will power the optical rise. Since we do not include breakout in our modeling (assumed to occur before observations began), the early-time light curve will be missed by the fit. After breakout, the cooling should still evolve according to the predictions of spherical or planar phase shock cooling, which are insensitive to the exact shape of the density profile (Rabinak & Waxman 2011; Sapir et al. 2011; Sapir & Waxman 2017). The parameter inference will likely be wrong in this case, since cooling is measured relative to the peak of breakout. A delay of $\delta t_{\rm d} = 0.12 \frac{\Delta R}{10^{13}\,{\rm cm}} \frac{v}{10^{9}\,{\rm cm\,s^{-1}}}^{-1}$day will result in an increase of $(1 + \delta t_{\rm d})^{1.8}$ in the fit progenitor radius but will not change the general conclusion that the radius is large enough to reach such a low $\rho_{\rm bo}$. This scenario is seemingly challenged by the lack of a strong association between the presence of flash ionization features and a large fit radius. However, flash features trace the CSM density profile at $\sim 10^{15}$ cm (Yaron et al. 2017) rather than the $R \sim 10^{14}$ cm required for this effect to become significant. This scenario is consistent with the conclusions of Morozova et al. (2018), who fit a grid of hydrodynamical models of progenitors surrounded by dense CSM at $<10^{14}$ cm and found that they are consistent with the light curves of observed SNe II, with breakout occurring at the edge of the dense CSM.

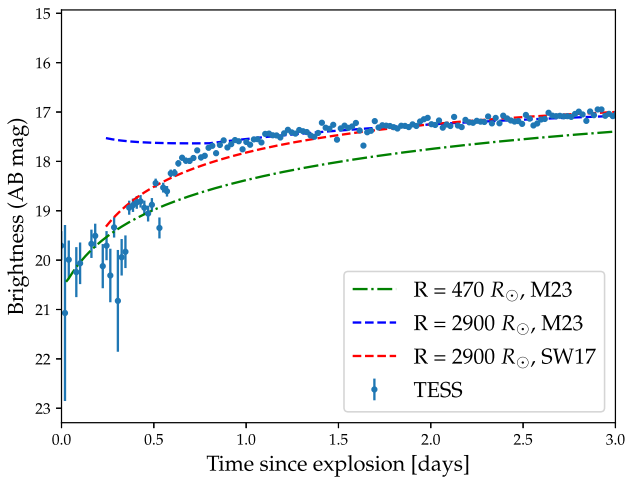

Figure 15. Best-fit shock-cooling models to the early-time TESS light curve of SN 2020nvm. The blue curve shows the best-fit M24 model to the multiband light curve, which misses the rise during the planar phase. The green curve shows the best fit for a narrow radius prior, and the red curve shows the same model as the blue curve but accounting only for the spherical phase with the model of Sapir & Waxman (2017). While assuming spherical phase evolution at all times can reproduce the full light curve, taking the planar phase into account results in a different early-time light curve. When including the planar phase, no good fit is found that can describe the entire light curve.

Similarly to the heating defining the extended breakout of the II-H category, an optical rise while the temperature is heating is the unambiguous marker of an increase in the bolometric luminosity, expected only during breakout itself. Observing or ruling out such heating during the first day of the explosion through high-cadence UV-optical observations thus has the potential to resolve any remaining ambiguity regarding SNe in the II-C- group, since all three options presented above have different predictions for the breakout pulse itself.

1. The breakout pulse occurs at densities of $\sim 10^{-9}$ g cm^{-3}. The breakout duration is likely dominated by the light travel time, lasting minutes to an hour. Breakout will likely peak at tens of eV.
2. The breakout pulse occurs at densities of $\sim 10^{-9}$ g cm^{-3}. The asymmetric nature of the breakout shell caused a smearing of the breakout to a timescale of a few hours. Locally, the width of the shock transition is still similar, so that breakout would still likely peak at tens of eV.
3. The breakout pulse occurs at densities of $\lesssim 10^{-11}$ g cm^{-3}. The low density causes the intrinsic breakout timescale to last a few hours, dominating over the light travel time. Locally, the width of the shock transition is large, so that breakout might be peaking at $\sim$10 eV and could contribute significantly to the optical during the early rise. No additional short-duration pulse can be observed.

5.1.2. The Intrinsic Progenitor Radius Distribution

To connect the observed parameter distribution to the intrinsic progenitor radius distribution, we account for the selection effects and biases introduced by our observation strategy and the dependence of the luminosity on the breakout radius. We calculate model light curves for the sample of RSGs of Davies et al. (2018). We calculate the radii from the observed effective temperatures and luminosities and generate

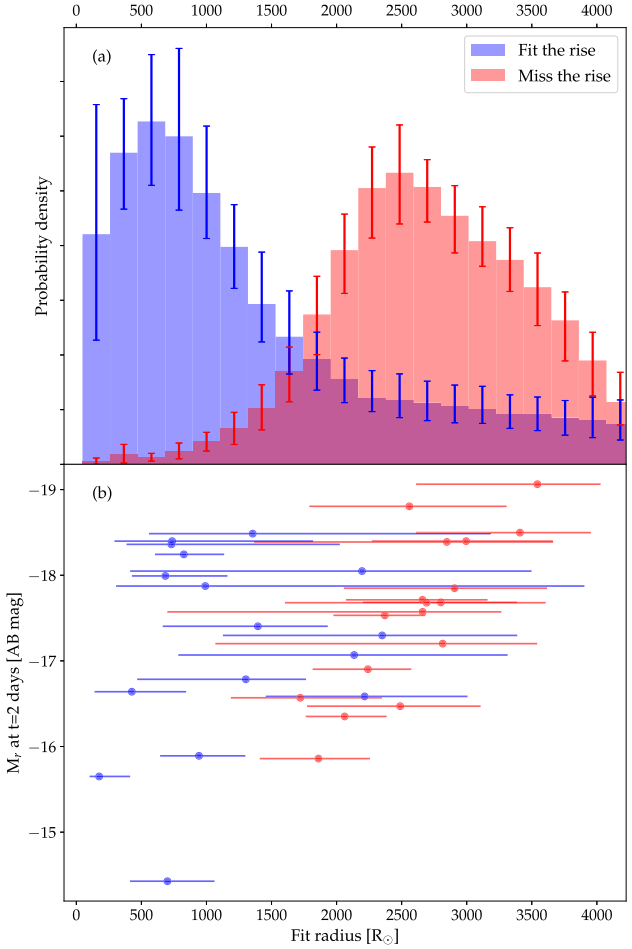

Figure 16. (a) Posterior probability distribution of the breakout radius for SNe whose fit misses the rise and SNe whose best fit does not miss the rise. (b) A scatter plot showing the correlation between the best-fit radius and the r-band magnitude at $t = 2$ days. A large fit radius is strongly associated with missing the rise during the first day and is associated with a brighter r-band light curve.

a set of light curves with a velocity parameter $v_{s*,8.5}$ in the range 0.5–1.5, with the rest of the model parameters set to unity and assuming no host or galactic extinction along the line of sight. We test what fraction of the models is recovered by our observation strategy as a function of distance, demanding a blue color ($g - r < 0$ mag) at $t = 1$ day and an object brighter than 19.5 mag at the same time, which is the typical brightness limiting our ability to classify the object as an SN II, a criterion for follow-up in our program. We repeat this analysis for an Ultraviolet Transient Astronomy Satellite (ULTRASAT) strategy, demanding an optical brightness above 19.5 mag at peak for spectroscopic classification, and that the light curve is higher than the *ULTRASAT* limiting magnitude of 22.5 mag at 1 day (Shvartzvald et al. 2024).

We find that as the distance increases above 70 Mpc, we are increasingly biased toward higher progenitor radii. In panel (a) of Figure 18, we show the fraction of RSG explosions recovered as a function of distance with each strategy and a histogram of the distances of our sample. In panel (b), we show the mean radius of the recovered sample as a function of distance. In panel (c), we show the posterior distribution of the SN radius above and below a distance of 70 Mpc. The radius posterior distribution of closer SNe is highly skewed toward

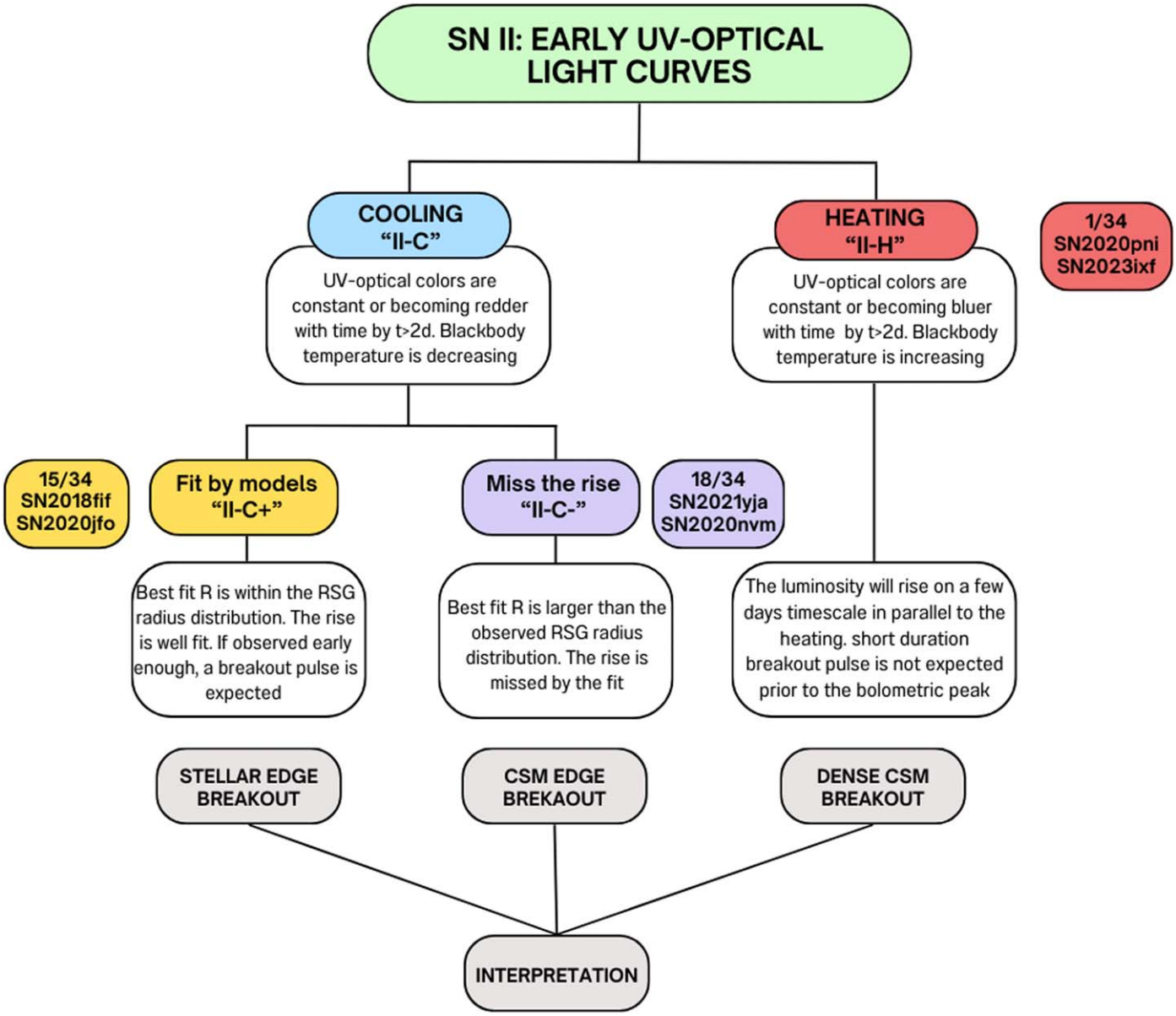

Figure 17. Schematic classification of the early light curves of SNe II. They are roughly divided into two groups: (1) SNe with increasing temperatures at early times, which we call "II-H," and (2) SNe with decreasing temperatures, or "II-C." We further divide the latter into two groups: (a) those that are well fit by shock-cooling models at early times and have a good early fit and a small fit radius (we call these "II-C+") and (b) those that are not well fit at early times, are more luminous as a population, and have larger fit radii (we call these "II-C-"). Next to each group, we denote the number of SNe in the sample that belong to it, as well as example SNe.

radii below 1000 $R_{\odot}$, while the distribution of SNe at larger distances is skewed to values above 1000 $R_{\odot}$.

We correct the Malmquist bias following the treatment of Rubin et al. (2016). For each point in the posterior sample, we calculate a weight factor $w_i = \frac{D_i^3}{\sum_j D_j^{-3}}$, where $M_i + 17 = 5\log(\frac{D_i^*}{/10\,\mathrm{pc}})$. We show the resulting corrected posterior distribution in Figure 18(d), along with the unweighted distribution and the distribution of RSG radii of Davies et al. (2018). The error bars are calculated by bootstrapping the posterior distribution: for every realization, we recalculate the posterior for 33 SNe randomly sampled from the list of SNe with viable fits, while allowing for repetition. We repeat this process 500 times and plot the mean and standard deviation on each bin of the histogram.

Our analysis shows that even if most (67^{+9}_{-5}%) of the observed SNe have large ($R > 1200\,R_{\odot}$) breakout radii, the breakout radius distribution would be consistent with the observed RSG radius distribution ($R < 1200\,R_{\odot}$) in 69^{+13}_{-26}% of SNe II explosions. K. Hinds et al. (2024, in preparation) analyzes the optical light curves of SNe II in the magnitude-limited BTS and reaches a similar conclusion. We further note that for SNe with a CSM breakout such as SN 2020pni, SN 2018zd, or SN 2023ixf, a breakout radius of $\sim$1500–3000 $R_{\odot}$ is needed to explain the breakout timescale and would be consistent with the distribution we report here (Zimmerman et al. 2024). In the case of SN 2023ixf, constraints on the SN progenitor from preexplosion data confirm a dusty shell at a similar radius (e.g., Qin et al. 2023). This supports the idea that SNe II-C- have large radii due to a shell of CSM from which shock breakout occurs.

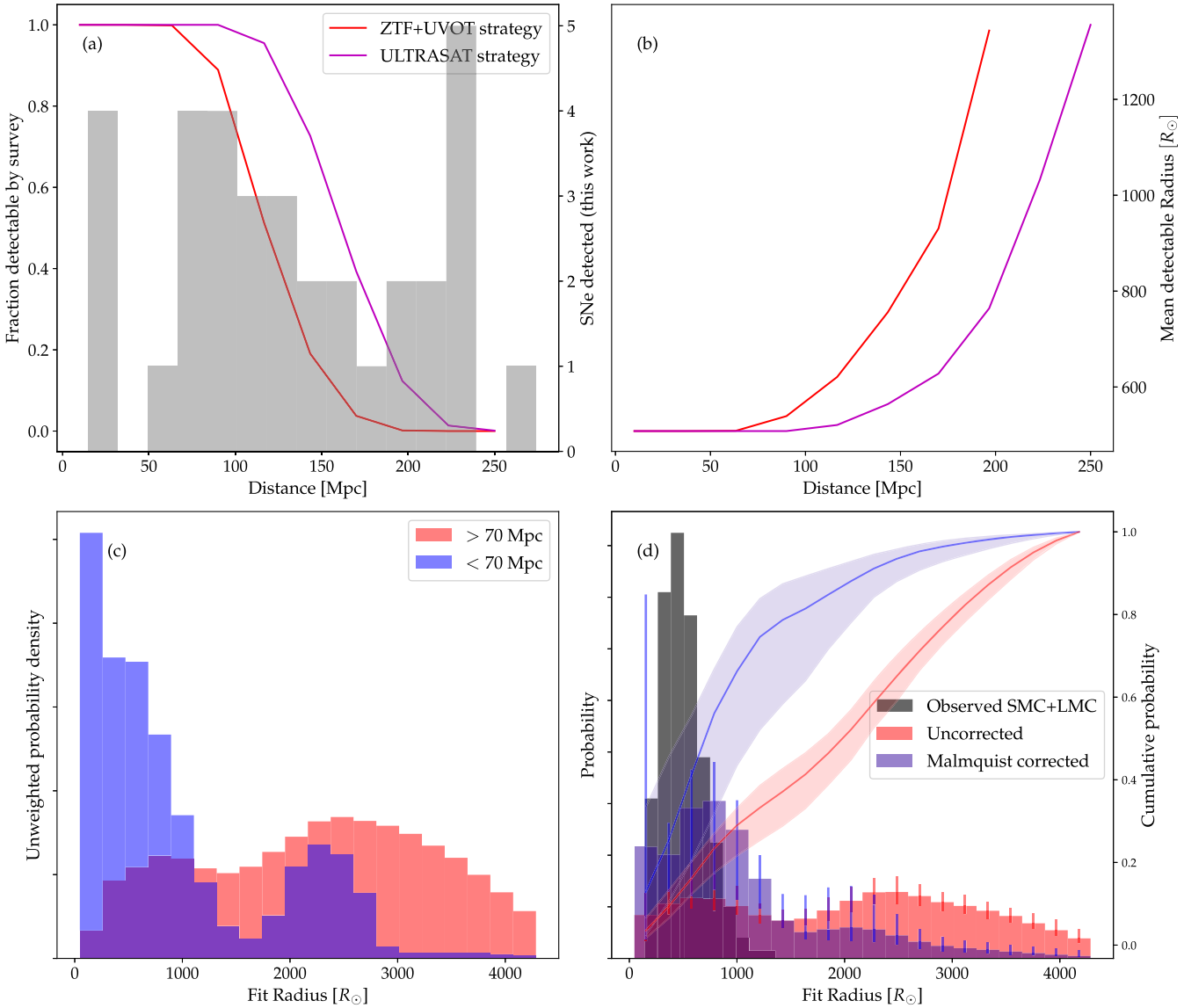

Figure 18. (a) A histogram of the distances of SNe in this work and the fraction of simulated SN light curves which would be followed up with our observations study, and in the ULTRASAT survey. We assume the radius distribution of Davies et al. (2013) for the models. (b) The mean radius of the detected SNe, demonstrating a luminosity bias at $d > 70$ Mpc. (c) The unweighted posterior probability distribution of the breakout radius and d above or below 70 Mpc. (d) The posterior distribution of the full sample, corrected and uncorrected for the luminosity bias. The gray histogram is a distribution of RSG radii from Davies et al. (2013). We also shock the cumulative distribution of the observed and corrected posterior distribution with 68% confidence intervals. While the observed fraction of SNe with a large $>1000\,R_\odot$ radius is 71^{+7}_{-4}%, they only account for 34^{+23}_{-11}% of exploding RSGs.

5.2. X-Ray Emission and Constraints on Extended CSM Density

Following SN shock breakout, the accelerated ejecta will expand into the surrounding optically thin CSM, acting as a piston and creating a shock in the CSM. For typical CSM densities, this shock is expected to be collisionless, heat the gas to $\sim$100 keV temperatures, and produce X-ray emission (Fransson et al. 1996; Katz et al. 2011; Chevalier & Irwin 2012; Svirski et al. 2012; Ofek et al. 2014). In Section 3.3, we reported the XRT detections and upper limits at the SN location, binned over the duration of the Swift observations (typically $\sim$10,000 ks). The limits we acquire are several orders of magnitude deeper than the optical emission, reaching as deep as a few SNe II previously detected by XRT: SN 2005cs (Brown et al. 2007), SN 2006bp (Brown et al. 2007), SN 2012aw (Immler & Brown 2012), SN 2013ej (Margutti et al. 2013), and, recently, SN 2023ixf (Grefenstette et al. 2023).

In Figure 19, we show the ratio of X-ray to UV-optical emission, measured at the same times and averaged over the duration of the Swift observations for the different SNe in our sample. Upperlimits range between 10^{-1} and 10^{-4} of the optical emission, and the highest detection is $\sim 10^{-2}$. In Section 4.3.2, we derived constraints on the velocity profiles of the SN ejecta through UV-optical light-curve fitting. The photon arrival weighted time of our detections (as well as those in the literature) typically correspond to a few days after explosion, probing the forward shock emission in the extended CSM around the progenitor star at $(0.5\text{–}2) \times 10^{15}$ cm. We can use these to constrain the CSM density at $\sim 10^{15}$ cm and subsequently constrain the mass loss of the progenitor star a few years prior to explosion.

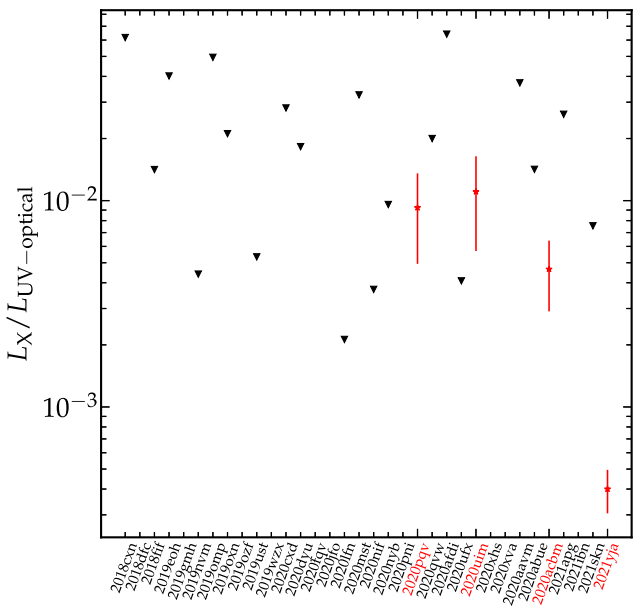

Figure 19. The ratio of X-ray to UV-optical emission, measured at the same times and averaged over the duration of the Swift observations for the different SNe in our sample. Upper limits are shown as black triangles, and the four detections we report are shown using red points.

At a time t, a constant velocity shock moving through an optically thin CSM with $v_{s,\rm csm}$ will sweep up a mass

$$\frac{M_{\rm CSM}}{M_\odot} = 2.7 \times 10^{-4}\, v_{s,\rm csm,9} t_{5d}\, \rho_{o,-16}, \quad (1)$$

where $v_{s,\rm csm,9} = \frac{v_{s,\rm csm}}{10^9\ {\rm cm\ s^{-1}}}$, $t_{5d} = \frac{t_{\rm xray}}{5\ {\rm d}}$, and $\rho_{o,-16} = \frac{\rho_o(r=10^{15}\ {\rm cm})}{10^{-16}\ {\rm g\ cm^{-3}}}$. To find the velocity $v_{s,\rm csm}$, we assume it is well approximated by the velocity of the piston (the ejected envelope) at equal mass to the swept-up CSM. This is given through the profiles of Rabinak & Waxman (2011). Following their notation (their Equations (3) and (4)), we find

$$\delta_{m,\rm piston} = \frac{M_{\rm csm}}{M_{\rm tot}} = 2.7 \times 10^{-4} \frac{f_\rho\, v_{s,\rm csm,9} t_{5d}\, \rho_{o,-16}}{f_\rho\, M_\odot}, \quad (2)$$

$$v_{s,\rm csm} = v_f \left(\delta_m = \frac{M_{\rm csm}}{M_{\rm tot}}\right). \quad (3)$$

As long as the fraction $\frac{M_{\rm CSM}}{M_{\rm tot}}$ is larger than the mass fraction in the breakout shell $\delta_{m,\rm bo}$,

$$\frac{v^{(1)}_{s,\rm csm}}{\rm cm\ s^{-1}} = 1.5 \times 10^9 \left(\frac{f_v}{2} v_{s*,8.5}\right)^{0.9} \left(\frac{t_{5d}\,\rho_{o,-16}}{f_\rho\, M_\odot}\right)^{-0.1}. \quad (4)$$

Here we took $f_v = \frac{v_f}{v_s} = 2$, which is typically the case for small $\delta_m < 0.01$ (Matzner & McKee 1999). This is in agreement with the velocity evolution of Chevalier & Fransson (1994) for a steep postshock ejecta density profile, as expected here (see, e.g., Waxman & Katz 2017, and references therein). If $\frac{M_{\rm csm}}{M_{\rm tot}} < \delta_{m,\rm bo}$, we can assume $v_f = f_v v_{s,\rm bo}$, which is the maximum velocity at which breakout occurs. In this case,

$$\frac{v^{(2)}_{s,\rm csm}}{\rm cm\ s^{-1}} = 2 \times 10^9 \left(\frac{f_v}{2}\right) (\kappa_{0.34} f_\rho M)^{0.13} (v_{s*,8.5})^{1.13} R_{13}^{-0.26} \quad (5)$$

so that $v_{s,\rm csm} = \min\,(v^{(1)}_{s,\rm csm},\ v^{(2)}_{s,\rm csm})$.

The total luminosity generated by the collisionless shock is given by $L(t) = 2\pi \rho_{\rm csm} r^2 v^3_{s,\rm csm}$.

Using the derived $v_{s,\rm csm}$, we find

$$L_{\rm X} = 10^{42}\ {\rm erg\ s^{-1}} \times \begin{cases} 2.1\ \rho^{0.7}_{o,-16} v^{2.7}_{s*,8.5} t^{-0.3}_{5d} (f_\rho M_{0,\odot})^{0.3} & v_{s,\rm csm} = v^{(1)}_{s,\rm csm} \\ 0.6\ \rho_{o,-16} (\kappa_{0.34} f_\rho M_{0,\odot})^{0.4} & \\ \quad \times (v_{s*,8.5})^{3.4} R_{13}^{-0.8} & v_{s,\rm csm} = v^{(2)}_{s,\rm csm} \end{cases}. \quad (6)$$

Using Equation (6), we convert our constraints on the XRT luminosity to constraints of the CSM density and mass loss. We assume a bremsstrahlung spectrum with a temperature $T = 200\mu \left(\frac{v_{s,\rm csm}}{10^9\ {\rm cm\ s^{-1}}}\right)^2$ keV (Fransson et al. 1996; Katz et al. 2011), where μ is the mean particle weight assumed to be $\mu = 0.61$ for an ionized medium with a solar composition. We then correct the observed XRT luminosity to a bolometric X-ray luminosity, with correction factors ranging from 2 to 6 over our sample. We assume no intrinsic X-ray absorption at the SN site. To estimate the error on the values, the calculation is repeated for 100 points randomly drawn from the posterior sample on the shock-cooling light-curve fits and by randomly drawing points from a Gaussian distribution with a mean and standard deviation representing the X-ray measurements. We calculate $\frac{\dot{M}}{M_\odot\,{\rm yr^{-1}}} = 10^{-4} \rho_{o,-16} v_{w,50}$, where $v_{w,50}$ is the CSM velocity in units of 50 km s^{-1}, assumed to be 1.

We show our constraints in Figure 20. Here the colored points represent individual detections, the black downward-pointing triangles represent upper limits, and the blue plus stands for the estimate of Grefenstette et al. (2023) for the mass loss of SN 2023ixf with a shock velocity arbitrarily chosen to be 10^9 cm s^{-1}, deduced from the absorbing hydrogen column density between subsequent observations.

There are two main systematics involved in our approach. (1) The emission spectrum of a shock traversing the CSM is highly uncertain, and assuming it will emit with a temperature equal to the plasma temperature is probably inaccurate. For example, Grefenstette et al. (2023) found for SN 2023ixf a temperature of 35^{+22}_{-12} keV, which results in a velocity $v = (0.54^{0.15}_{-0.1}) \times 10^9$ cm s^{-1}, which is lower by at least a factor of 2 from the observed photospheric velocity of SN 2023ixf (Jacobson-Galán et al. 2023; Zimmerman et al. 2024). Decreasing the temperature of the X-ray spectrum from >120 keV to 35 keV would reduce the bolometric X-ray luminosity by factor of >2 and subsequently reduce the mass loss and density. (2) The intrinsic absorption of the CSM could affect the emission. In the case of SN 2023ixf, Grefenstette et al. (2023) report an absorption column density of $2.6 \sim 10^{23}$ atoms cm^{-2} at $t = 4$ days and $5 \sim 10^{22}$ atoms cm^{-2} at $t = 11$ days. Using the NASA Portable, Interactive Multi-Mission Simulator,[24] we estimate that our results would change by a factor of $\times 2$ if $N_{\rm H} = 1 \times 10^{23}$ cm^{-2} in the XRT band. Such a value at the typical photon-weighted XRT observation time would imply a mass-loss rate of $\gtrsim 10^{-4} M_\odot\ {\rm yr^{-1}}$, indicating that this will affect only a few of the SNe in our sample. Our limits are consistent with the observed mass loss of field RSGs (de Jager et al. 1988; Marshall et al. 2004; van Loon et al. 2005) but lower than inferred through modeling of narrow "flash ionization" spectral features, implying mass-loss rates as

[24] https://heasarc.gsfc.nasa.gov/cgi-bin/Tools/w3pimms/w3pimms.pl

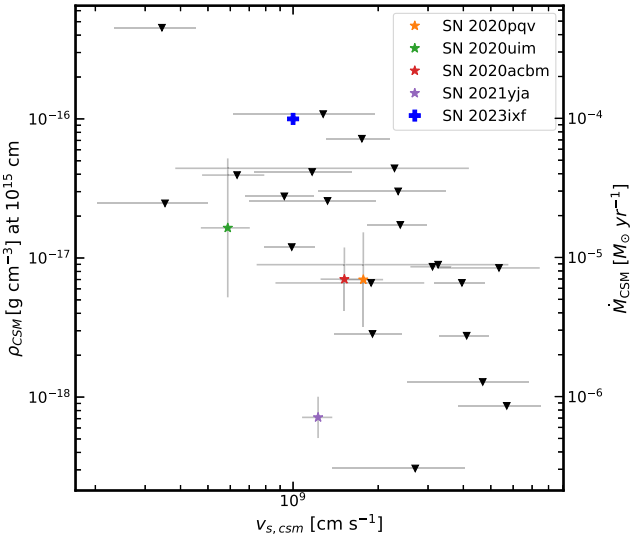

Figure 20. X-ray limits on the extended ($\sim 10^{15}$ cm) CSM density, mass loss, and CSM shock velocity. Black downward-pointing triangles represent upper limits, colored points are detections from this work, and the blue plus represents the X-ray constraints of SN 2023ixf from Grefenstette et al. (2023). The extended 10^{15} cm mass loss is consistent with field RSG levels.

high as $10^{-2}\ M_\odot\,\mathrm{yr}^{-1}$ (Dessart et al. 2017; Boian & Groh 2019), likely since these methods probe different regions of the CSM density profile. This is also the case for SN 2023ixf: comparisons of the early-time spectra performed by Jacobson-Galán et al. (2023) and Bostroem et al. (2023b) to the models of Dessart et al. (2017) indicate a mass-loss rate of 10^{-3}–$10^{-2}\,M_\odot\,\mathrm{yr}^{-1}$, much higher than those inferred by Grefenstette et al. (2023) probing the extended CSM. The models of Dessart et al. (2017) introduce a mass-loss rate declining continuously to $10^{-6}\,M_\odot\,\mathrm{yr}^{-1}$ by $r = 10^{15}$ cm, reflecting a dense mass-loss region swept up by the shock in the CSM at early times. Thus, they are capable of discriminating between different CSM densities at a few 10^{14} cm.

Since some amount of confined CSM is present in the majority of SNe II (Bruch et al. 2021), we consider the effect of such dense CSM on our analysis. We repeat the analysis but assume that the CSM swept up by the shock at $t < t_X$ has a density profile of 10^{-14} g cm$^{-3}\left(\frac{r}{10^{15}\,\mathrm{cm}}\right)^{-2}$ ($\dot{M} = 10^{-3} M_\odot\ \mathrm{yr}^{-1}$). This weakly decreases v_{csm} and subsequently decreases L. For the majority of the sample, our limits do not change by more than 50%, and at most by a factor of 3.

Our results independently support the conclusion that by $\sim 10^{15}$ cm, the density of the CSM has already declined to the typical values observed for RSG stars, and that regions of dense mass loss are confined to the nearby environment of the progenitor star and probing the final year of its evolution.

5.3. Observing Shock Breakout and Shock Cooling with ULTRASAT

ULTRASAT will conduct a high-cadence (5 minutes) UV survey with a 200 deg^2 field of view. It will detect tens of shock-breakout signatures and hundreds of shock-cooling light curves in its first 3 yr (Shvartzvald et al. 2024). The high-cadence light curves of ULTRASAT will resolve all phases of the early SN evolution—shock breakout, planar phase, and spherical phase shock cooling. While spherical shock cooling alone provides constraints on the progenitor parameters, the planar phase, typically lasting hours, can discriminate between models more finely. Directly observing the breakout pulse can provide independent constraints on the breakout radius and the velocity of the outermost layers of the ejecta. This can resolve the remaining ambiguity as to the reason for the systematic deviation from the expected planar phase in large-radius fits. Observing the early UV-optical color of SNe will discriminate between a light-curve rise driven by cooling following a stellar edge breakout or by heating of the ejecta during an extended shock breakout in a shallow density profile (examples of the latter include SN 2020pni, SN 2018zd, and SN 2023ixf). For SNe with light curves well matched by a stellar breakout, the velocity and mass of the breakout shell will be constrained by the breakout pulse itself (Sapir et al. 2011, 2013).

In combination with X-ray follow-up and spectral modeling, these can be used to accurately map the CSM density profile, with each tracer probing a different segment of the density profile. While there have been some candidate shock-breakout flares in the optical (Garnavich et al. 2016; Bersten et al. 2018), some claims have been disputed (Rubin & Gal-Yam 2017), and the sample of TESS core-collapse SNe of Vallely et al. (2021), binned to 30 minutes cadence, shows no detection of breakout flares. Breakout flares are expected to peak in the UV or X-ray, but the non-LTE spectral shape makes prediction in the optical highly uncertain (Sapir et al. 2013; Sapir & Halbertal 2014). While initially the number of photons produced is not enough to reach thermal equilibrium, the planar phase temperatures are already close to the equilibrium temperature, and the exact details of this transition can change the optical light curve by orders of magnitude. The UV peak, closer to the peak frequency of the emission, is much better understood.

In order to produce a clear prediction for the ULTRASAT survey based on the observed sample of SNe II, we calculate the breakout signal in TESS and in the UVOT UVM2 bandpass (UVM2 is chosen since it is closest to the ULTRASAT bandpass). For every SN we fit in Section 4.3, we use breakout properties ρ_{bo} and $v_{s,\mathrm{bo}}$ to calculate the luminosity and spectrum at breakout according to the models of Sapir et al. (2011, 2013) and Katz et al. (2012). We integrate the spectrum and compute the typical TESS and ULTRASAT brightness during breakout and the duration of the expected breakout. We show the distribution of parameters in Figure 21. Panel (a) shows a kernel density estimate (KDE) plot of the ULTRASAT breakout landscape, and panel (b) shows the expected TESS brightness. We highlight the predictions for SN 2020fqv and SN 2020nvm, observed by TESS. We stress that the optical wavelength predictions are highly uncertain and should be treated as lower limits. Our results are consistent with the entirety of the breakout flares predicted by our modeling being measured by ULTRASAT and none of the flares being observed in the optical wavelengths.

6. Conclusions and Summary

1. In this paper, we have presented the UV-optical photometry of 34 spectroscopically regular SNe II detected in the ZTF survey and followed up by the Swift telescope within 4 days of explosion. In addition to the UV-optical data, we report four XRT detections and 3σ upper limits for the rest of the sample.
2. In Section 4.1, we analyze the color evolution of the sample. We show that besides SN 2020pni, the rest of our sample had UV-optical colors that are becoming redder

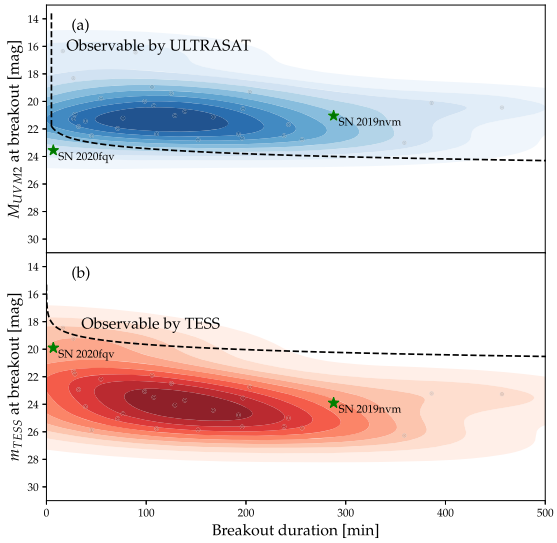

Figure 21. Prediction for the breakout flare signal from a sample of SNe II in the optical and UV. Panel (a) shows a KDE plot of the ULTRASAT breakout duration and peak magnitude. Gray points correspond to the prediction of the best-fit cooling light curve. The dashed line shows the limiting magnitude of the survey binned to varying degrees. Panel (b) shows the same for the TESS bandpass, although the predictions for the breakout pulse spectrum are less certain in the optical and should be treated as lower limits. Our results show that it is very difficult to rule out the existence of a breakout pulse in optical wavelengths alone.

with time across the entire SED, indicating that they are cooling.

3. We show that the combination of UV, UV-optical, and optical colors can be used as a discriminator between various degree of intrinsic time-dependent deviations from blackbody and host-galaxy extinction with non–Milky Way extinction laws. We show that there is no preference in UV-optical color for SNe with flash features and argue that the deviations are consistent with the predictions of shock-cooling models.
4. Using the scatter in early-time color, we argue that our sample has a host extinction smaller than $E(B-V) = 0.2$ mag. Subsequently, we show we can measure the extinction of highly extinguished SNe to better than 0.2 mag. The average early-time colors of the SNe in our sample are provided in Table 5.
5. In Section 4.2, we fit the SEDs of the SNe in our sample to a blackbody at the times of UVOT observations and recover the evolution of the blackbody radius and temperature. We show that the evolution of these parameters is in excellent agreement with the predictions of spherical phase shock cooling, with a statistically significant difference in the average temperature and radius between objects with and without flash features. We also show that at least 30% of the objects in our sample are more luminous than expected from an envelope breakout with $R < 10^{14}$ cm, indicating a larger progenitor radius or a higher shock velocity parameter relative to generic expectations.
6. Motivated by the good agreement with the predictions of spherical phase shock cooling, we present a method to fit the light curves to the latest shock-cooling models in Section 4.3.1, accounting for deviations from the blackbody over a large range of parameters and interpolating between the planar and spherical phase of shock cooling. We demonstrate that this method is unbiased when fitting the multigroup simulations of M24, although these have correlated residuals. We demonstrate that we can recover the breakout radius R_*, the shock velocity parameter $v_{*,8.5}$ describing the velocity profile in the outer regions of the ejecta, and the extinction. We show that we cannot recover the envelope mass $M_{\rm env}$, total mass M, or numerical density scaling parameter f_ρ using our method. We conclude that by fitting, we can confirm or reject the underlying assumption of shock cooling following envelope breakout.
7. Overall, we find that the early UV-optical light curves of our sample are divided into three groups. (1) A majority (33/34) of SNe that cool at early times, which we denote as "II-C." This group is comprised of (a) SNe that are well fit throughout their evolution, with radii characteristic of the observed RSG radius distribution, and (b) SNe that are fit by larger-radius, more luminous models and that systematically miss the early (<1 day) rise. We denote these as "II-C+" and "II-C-," respectively. (2) The third group is represented by a single object in our sample (SN 2020pni), which is heating in the first few days. A similar evolution has been observed for the nearby SN 2023ixf and for SN 2018zd. We denote these as "II-H."
8. As we have demonstrated that there is no bias in our fitting method, we argue that this deviation from the predicted rise reflects a physical difference from an idealized breakout from a polytropic envelope. We speculate that this difference could be related to the presence of CSM or an asymmetric shock breakout. We assume the inference of large radii is real and show that while most of the sample is characterized by a large radius, this is due to a luminosity bias affecting our sample at a distance of >70 Mpc. We show the volume-corrected probability peaks at radii similar to those of field RSGs. We conclude that while 71^{+7}_{-4}% of observed SNe II are overluminous, with a large radius, the majority (66^{+11}_{-22}%) of exploding RSGs have a typical radius at explosion. Since some objects in our sample are also consistent with a smaller radius, this should be treated as a lower limit.
9. Using the X-ray limits and the constraints on the velocity profile of the ejecta from the light-curve fitting, we derive limits on the CSM density at 0.5–2 $\times 10^{15}$ cm from the progenitor star, which constrains the mass loss of the progenitors ~3–15 yr before the explosion assuming 50 km s^{-1} winds. We show that the limits and detection are systematically lower than the required mass loss to explain flash ionization features, supporting the conclusion that these stars undergo increased mass loss in the final months before explosion. Uncertainties in the spectral shape of the X-ray emission, the amount of CSM below 10^{14} cm, and absorption in the CSM will change this result by less than an order of magnitude.
10. In Section 5.3, we study the predictions of the fit parameter distribution to the landscape of shock-breakout flares for the ULTRASAT mission and high-cadence optical missions such as TESS. We argue that the nondetections of breakout flares in the optical surveys are to be expected, and that observations with ULTRASAT should indeed easily discover the breakout flares from an analog sample to ours.

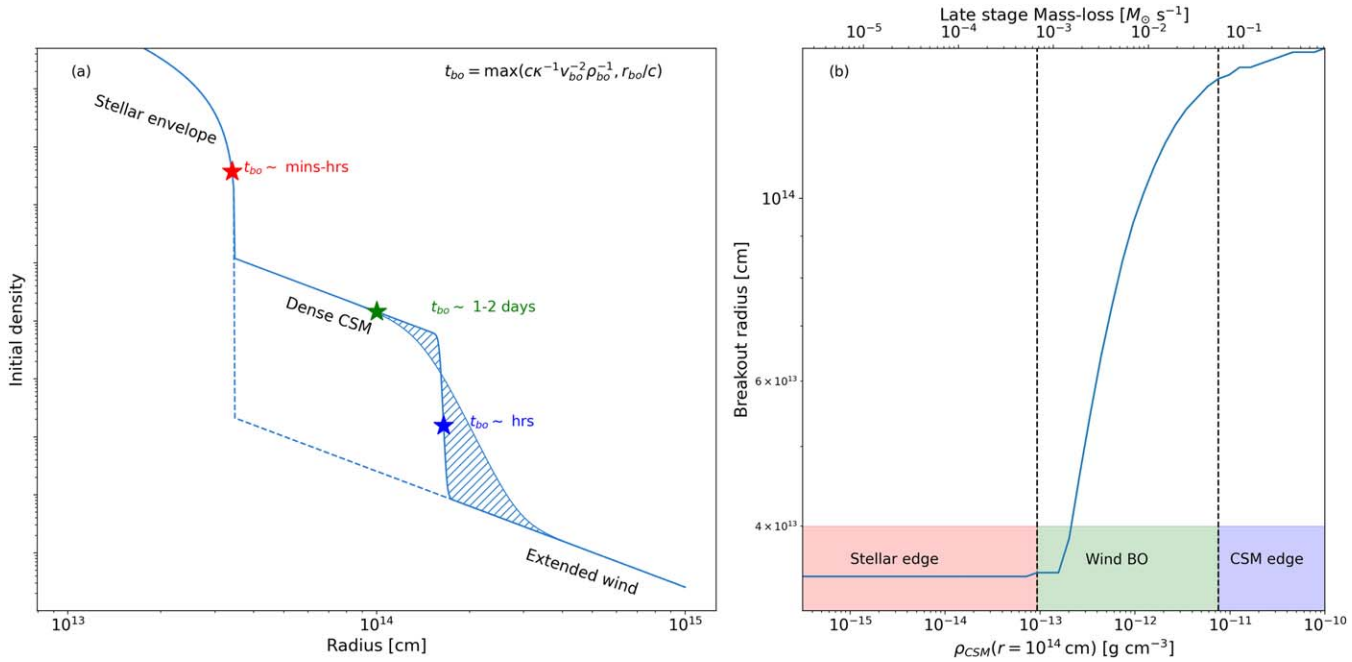

Figure 22. (a) Schematic illustration of the proposed alternatives for early observations of SNe II. The curves represent possible preexplosion density profiles of the envelope and CSM, corresponding to the mass-loss history of the progenitor in the months before explosion. Depending on the exact parameters of this profile, the breakout shell can be located in three possible locations. The red star represents a breakout radius at the edge of the stellar envelope. Since the density is steeply declining, the shock transition region is narrow, and the duration of breakout will be typically dominated by the light travel time. The blue star corresponds to a breakout at the edge of a dense shell of CSM. The density profile is declining steeply, and the breakout pulse duration can be set either by the light travel time or by the shock crossing time, both lasting hours. The green star corresponds to the third option, occurring for a minority of cases. Here the density profile is shallow and increasing the duration of the breakout pulse to the shock crossing timescale of a few days. The $r \lesssim 3 \times 10^{14}$ cm density will determine the early light curve and spectra, and the $r \gtrsim 3 \times 10^{14}$ cm density determines the X-ray emission emerging after the first few days. (b) The breakout radius for a star with a 500 $R_\odot$ and 1 $M_\odot$ stellar envelope surrounded by varying amounts of CSM confined to 1.5×10^{14} cm. The conversion to mass loss assumed $v_w = 50$ km s^{-1}. Increasing the mass of the shell of dense CSM moves the breakout location from the stellar envelope, to the shallow region of the dense CSM, and onward to the edge of the dense CSM if a significant portion of the envelope was ejected.

11. By combining our constraints on the breakout radius and the extended CSM density, we propose a scenario that explains all three groups in our sample in a single framework. By varying the amount of CSM lost in the last year, the breakout radius, duration, and temperature change. If a small amount of mass ($\lesssim 10^{-3}\,M_\odot$) is lost, breakout will occur at the stellar envelope. Its characteristic duration will be minutes to an hour and will peak in the extreme UV. This scenario can explain most SNe II-C+. If the star loses most of its envelope ($\gtrsim 0.1\,M_\odot$), breakout will occur at the edge of the dense CSM. The characteristic breakout duration will be hours long and can contaminate the early light curves, as it will peak in the far-UV. This scenario will explain most II-C-. If the SN loses $\sim 0.01\,M_\odot$ during the last year, breakout will occur in the dense CSM. Such a breakout will occur over a timescale of a few days, during which heating of the breakout region and an increase in luminosity will be observed as the breakout pulse is released, with an SED peaking in the near-UV. This scenario will account for SNe II-H. This framework is schematically summarized in Figure 22.

Acknowledgments

We thank Doron Kushnir, Barak Zackay, and Boaz Katz for their insights on the analysis. We are grateful to the staff at the various observatories where data were obtained. This work made use of data supplied by the UK Swift Science Data Centre at the University of Leicester.

Based on observations obtained with the Samuel Oschin Telescope 48 inch and the 60 inch telescope at the Palomar Observatory as part of the Zwicky Transient Facility project. ZTF is supported by the National Science Foundation under grant Nos. AST-1440341 and AST-2034437 and a collaboration including current partners Caltech, IPAC, the Weizmann Institute of Science, the Oskar Klein Center at Stockholm University, the University of Maryland, Deutsches Elektronen-Synchrotron and Humboldt University, the TANGO Consortium of Taiwan, the University of Wisconsin at Milwaukee, Trinity College Dublin, Lawrence Livermore National Laboratories, IN2P3, the University of Warwick, Ruhr University Bochum, and Northwestern University and former partners the University of Washington, Los Alamos National Laboratories, and Lawrence Berkeley National Laboratories. Operations are conducted by COO, IPAC, and UW.

The ZTF forced-photometry service was funded under Heising-Simons Foundation grant No. 12540303 (PI: M. J. Graham). The SED Machine at Palomar Observatory is based upon work supported by the NSF under grant 1106171. The Gordon and Betty Moore Foundation, through both the Data-Driven Investigator Program and a dedicated grant, provided critical funding for SkyPortal.

The Liverpool Telescope is operated on the island of La Palma by Liverpool John Moores University in the Spanish Observatorio del Roque de los Muchachos of the Instituto de Astrofísica de Canarias with financial support from the UK

Science and Technology Facilities Council. Partly based on observations made with the Nordic Optical Telescope, operated at the Observatorio del Roque de los Muchachos.

This research has made use of the Spanish Virtual Observatory (https://svo.cab.inta-csic.es) project funded by MCIN/AEI/10.13039/501100011033/ through grant PID2020-112949GB-I00 A.G.-Y.'s research is supported by the EU via ERC grant 725161, the ISF GW excellence center, an IMOS space infrastructure grant, and BSF/Transformative and GIF grants, as well as the André Deloro Institute for Advanced Research in Space and Optics, the Helen Kimmel Center for Planetary Science, the Schwartz/Reisman Collaborative Science Program, and the Norman E. Alexander Family Foundation ULTRASAT Data Center Fund, Minerva and Yeda-Sela; A.G.-Y. is the incumbent of the Arlyn Imberman Professorial Chair. E.W.'s research is partially supported by grants from the ISF, the Norman E Alexander Family M Foundation ULTRASAT Data Center Fund, the Nella and Leon Benoziyo Center for Astrophysics, the Schwartz Reisman Institute for Theoretical Physics, and the Max Planck Professorial Chair of Quantum Physics. E.O.O. is grateful for the support of grants from the Benozio center, the Willner Family Leadership Institute, Ilan Gluzman (Secaucus, NJ), Madame Olga Klein—Astrachan, the Minerva Foundation, the Israel Science Foundation, BSF-NSF, the Israel Ministry of Science, Yeda-Sela, Weizmann-MIT, and the Rosa and Emilio Segre Research Award.

Facilities: PO:1.2m, Swift (UVOT, XRT), PO:1.5m (RC), Liverpool Telescope (IO:O).

Software: `Astropy` (Astropy Collaboration et al. 2013, 2018), `IPython` (Perez & Granger 2007), `Matpotlib` (Hunter 2007), `Numpy` (Harris et al., 2020), `Scipy` (Virtanen et al. 2020), `exctinction` (Barbary 2016), `dynesty` (Skilling 2004, 2006; Feroz et al. 2009; Higson et al. 2019; Speagle 2020), GROWTH marshal (Kasliwal et al. 2019), Fritz/`SkyPortal` (van der Walt et al. 2019; Coughlin et al. 2023), `SWarp` (Bertin 2010).

Data Availability

All data used in this paper will be made available via WISeREP[25] (Yaron & Gal-Yam 2012). We make all figures of all light-curve fits and light-curve plots available. The code used for producing light-curve and blackbody fits is released to https://github.com/idoirani (Irani et al. 2024b).

Appendix

A.1. Shock-cooling Model

A.1.1. Blackbody Evolution

We fit SN light curves to the shock-cooling model of M23. This model describes the blackbody evolution of a cooling envelope until recombination or sufficient transparency of the envelope using a set of four free parameters: (1) R_{13}, the radius of the progenitor star in units of 10^{13} cm; (2) $f_\rho M_0$, the product of the numeric factor f_ρ, which describes the structure of the density near the edge of the stellar envelope, and M_0, which is the progenitor mass prior to the SN in units of $M_\odot$; (3) $v_{s*,8.5}$, the shock velocity parameter in units of $10^{8.5}$ cm s^{-1}, which corresponds to $v_{s*,8.5}=1.05 f_\rho^{-0.19}\sqrt{(E/M)}$, roughly equal to $\sim v_{\rm ej}/5$ at early times; and (4) $M_{\rm env}$, the envelope mass. $\kappa_{0.34}$ is the opacity in units of 0.34 cm^2 g^{-1} and is set to 1 for all cases. $t_{\rm d}/t_{\rm hr}$ is the time since the explosion in units of days or hours, respectively. Following their notation, L and T evolve according to

$$L_{\rm SC}=L_{\rm planar}+0.9\exp\left[-\left(\frac{2t}{t_{\rm tr}}\right)^{0.5}\right]L_{\rm RW}, \quad \text{(A1)}$$

$$T_{\rm col}=1.1\min\left[T_{\rm ph,planar},\,T_{\rm ph,RW}\right], \quad \text{(A2)}$$

which are valid during

$$3R/c=17\,R_{13}\,\min<t<\min[t_{0.7\,\rm eV},\,t_{\rm tr}/2]. \quad \text{(A3)}$$

The terms in Equations (A1)–(A3) are

$$\frac{L_{\rm planar}}{10^{42}\ {\rm erg\ s^{-1}}}=3.01\,R_{13}^{2.46}v_{s*,8.5}^{0.60}(f_\rho M_0)^{-0.06}t_{\rm hr}^{-4/3}\kappa_{0.34}^{-1.06}, \quad \text{(A4)}$$

$$\frac{T_{\rm ph,planar}}{\rm eV}=6.94\,R_{13}^{0.12}v_{s*,8.5}^{0.15}(f_\rho M_0)^{-0.02}\kappa_{0.34}^{-0.27}t_{\rm hr}^{-1/3}, \quad \text{(A5)}$$

$$\frac{L_{\rm RW}}{2.08\times10^{42}\ {\rm erg\ s^{-1}}}=R_{13}v_{s*,8.5}^{1.91}(f_\rho M_0)^{0.09}\kappa_{0.34}^{-0.91}t_{\rm d}^{-0.17}, \quad \text{(A6)}$$

$$\frac{T_{\rm ph,RW}}{\rm eV}=1.66\,R_{13}^{1/4}v_{s*,8.5}^{0.07}(f_\rho M_0)^{-0.03}\kappa_{0.34}^{-0.28}t_{\rm d}^{-0.45}, \quad \text{(A7)}$$

$$t_{0.7\rm eV}=6.86\,R_{13}^{0.56}v_{s*,8.5}^{0.16}\kappa_{0.34}^{-0.61}(f_\rho M_0)^{-0.06}\ {\rm days}, \quad \text{(A8)}$$

$$t_{\rm tr}=19.5\sqrt{\frac{\kappa_{0.34}M_{\rm env,0}}{v_{s*,8.5}}}\ {\rm days}. \quad \text{(A9)}$$

A.1.2. Deviations from the Blackbody

M24 fully relax the assumption of LTE. A temperature-, density-, and wavelength-dependent opacity is used to estimate the flux in every wavelength, accounting for the effects of line emission and absorption. A semianalytical model of the SED is calibrated to a set of radiation-hydrodynamical simulations with multiple photon groups. M24 show that the SED can be described using

$$L_\nu=\begin{cases}\left[L_{\rm BB}(0.85\,T_{\rm col})^{-m}+L_{\nu,\epsilon}^{-m}\right]^{-1/m} & h\nu<3.5T_{\rm col}\\ 1.2\times L_{\rm BB}(0.85R_{13}^{0.13}t_{\rm d}^{-0.13}\times T_{\rm col}) & h\nu>3.5T_{\rm col},\end{cases} \quad \text{(A10)}$$

with $m=5$ and

$$L_{\rm BB}=L\times\pi B_\nu(T_{\rm col})/\sigma T_{\rm col}^4, \quad \text{(A11)}$$

$$L_{\nu,\epsilon}=\frac{(4\pi)^2}{\sqrt{3}}r_{{\rm col},\nu}^2\frac{\sqrt{\epsilon_\nu}}{1+\sqrt{\epsilon_\nu}}B_\nu(T_{{\rm col},\nu}),\qquad \epsilon_\nu=\frac{\kappa_{{\rm ff},\nu}}{\kappa_{{\rm ff},\nu}+\kappa_{\rm es}}, \quad \text{(A12)}$$

and

$$r_{{\rm col},\nu}=R+2.18\times10^{13}L_{\rm br,42.5}^{0.48}T_{\rm br,5}^{-1.97}\kappa_{0.34}^{-0.07}\tilde{t}^{0.80}\nu_{\rm eV}^{-0.08}\ {\rm cm}, \quad \text{(A13)}$$

$$T_{{\rm col},\nu}=5.47\,L_{\rm br,42.5}^{0.05}T_{\rm br,5}^{0.92}\kappa_{0.34}^{0.22}\tilde{t}^{-0.42}\nu_{\rm eV}^{0.25}\ {\rm eV}, \quad \text{(A14)}$$

$$\kappa_{\rm ff}=0.03\,L_{\rm br,42.5}^{-0.37}T_{\rm br,5}^{0.56}\kappa_{0.34}^{-0.47}\tilde{t}^{-0.19}\nu_{\rm eV}^{-1.66}\ {\rm cm^2\ g^{-1}}. \quad \text{(A15)}$$

[25] https://www.wiserep.org

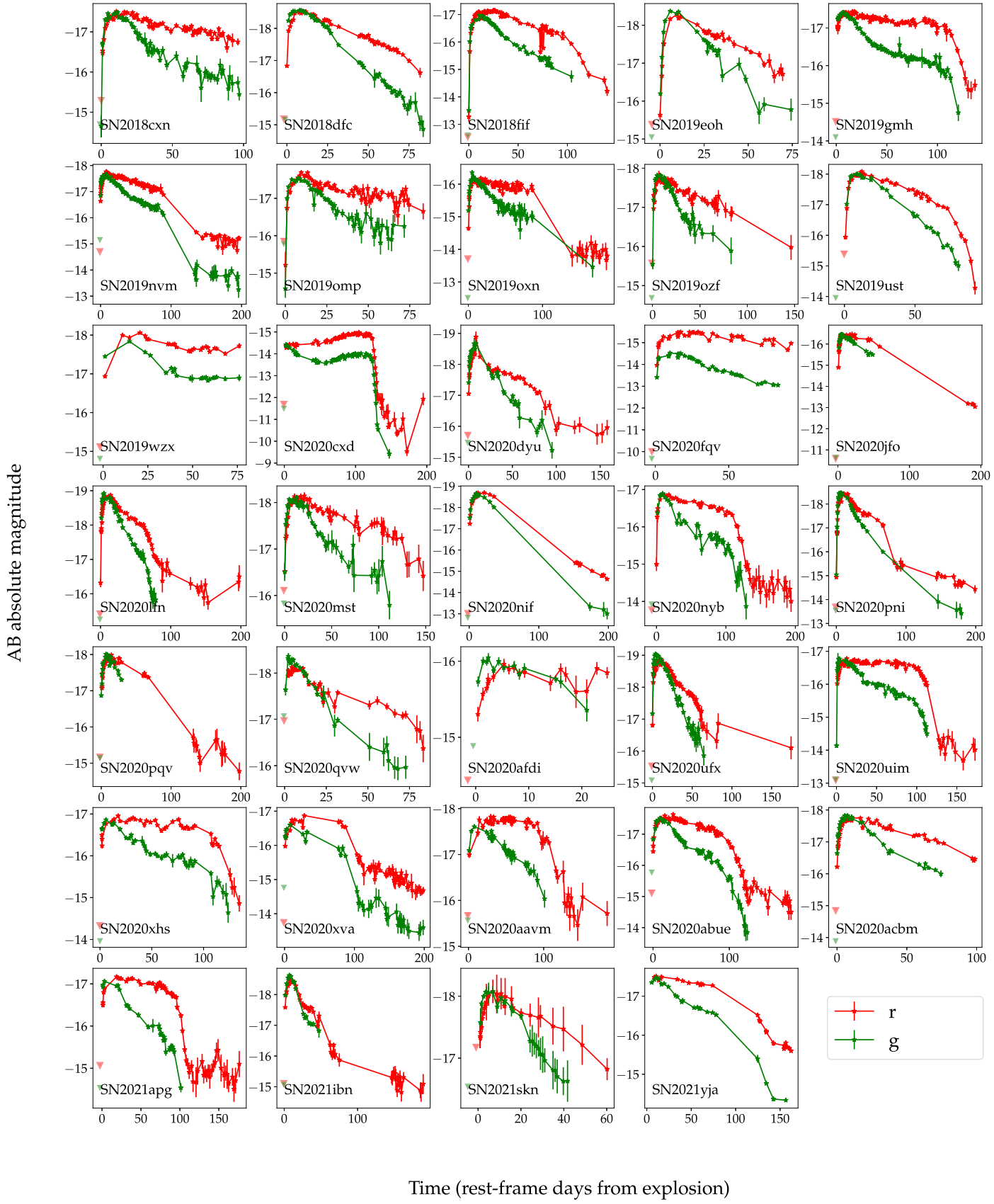

Figure 23. The full ZTF *g*-band and *r*-band light curves of our sample of 34 SNe II.

Table 5
SNe II Early-time Colors

t (rest-frame days)	Filter	λ_{piv} (Å)	W_{eff} (Å)	Mean $m_\lambda - m_r$ (mag)	STD (mag)	Bluest Color (mag)	Reddest Color (mag)	N_{SN}
1	UVW2	2055	305	−0.70	0.27	−1.13	−0.49	5
1	UVM2	2246	259	−0.70	0.30	−1.12	−0.32	5
1	UVW1	2580	397	−0.57	0.25	−0.97	−0.35	5
1	*u*	3467	352	−0.53	0.20	−0.82	−0.34	5
1	*g*	4702	641	−0.24	0.09	−0.43	−0.05	18
1	*i*	7489	767	0.27	0.15	0.14	0.60	6
2	UVW2	2055	305	−0.67	0.27	−1.30	−0.18	23
2	UVM2	2246	259	−0.64	0.28	−1.23	−0.02	22
2	UVW1	2580	397	−0.59	0.22	−1.17	−0.20	23
2	*u*	3467	352	−0.59	0.21	−0.95	−0.12	23
2	*g*	4702	641	−0.27	0.11	−0.44	0.06	30
2	*i*	7489	767	0.27	0.23	0.08	0.98	22
3	UVW2	2055	305	−0.33	0.30	−0.89	0.24	30
3	UVM2	2246	259	−0.37	0.30	−0.94	0.14	30
3	UVW1	2580	397	−0.36	0.24	−0.93	0.12	30
3	*u*	3467	352	−0.45	0.24	−1.05	0.16	30
3	*g*	4702	641	−0.18	0.12	−0.45	0.10	31
3	*i*	7489	767	0.23	0.21	0.00	0.93	25
4	UVW2	2055	305	−0.01	0.35	−0.57	0.68	29
4	UVM2	2246	259	−0.13	0.31	−0.71	0.39	29
4	UVW1	2580	397	−0.17	0.28	−0.73	0.29	29
4	*u*	3467	352	−0.34	0.25	−1.01	0.28	30
4	*g*	4702	641	−0.14	0.10	−0.39	0.02	31
4	*i*	7489	767	0.23	0.15	−0.02	0.80	24
5	UVW2	2055	305	0.31	0.35	−0.29	0.98	27
5	UVM2	2246	259	0.13	0.29	−0.45	0.62	26
5	UVW1	2580	397	0.01	0.22	−0.45	0.47	28
5	*u*	3467	352	−0.25	0.21	−0.51	0.41	28
5	*g*	4702	641	−0.12	0.09	−0.28	0.10	29
5	*i*	7489	767	0.21	0.10	−0.00	0.42	23

Here $L_{br} = L_{br,42.5} 10^{42.5}$ erg s^{-1}, $T_{col} = 5T_{col,5}$ eV, and $\nu = \nu_{eV}$ eV, and R in terms of the break parameters is

$$R = 2.41 \times 10^{13}\, t_{br,3}^{-0.1}\, L_{br,42.5}^{0.55}\, T_{br,5}^{-2.21} \text{ cm}. \quad \text{(A16)}$$

A.1.3. Fitting Procedure

Since the validity of this model is dependent on the model parameters, a χ^2 minimization is not applicable. Instead, we fit this model with a likelihood function adapted for a variable validity domain, as discussed in detail in Soumagnac et al. (2020):

$$\mathcal{L} = \text{PDF}(\chi^2, \text{dof}) = \frac{(\chi^2)^{\frac{N}{2}-1} \exp\left(\frac{\chi^2}{2}\right)}{2^{\frac{N}{2}}\Gamma\left(\frac{N}{2}\right)}, \quad \text{(A17)}$$

where χ^2 is the χ^2 statistic, the pdf is the χ^2 distribution given the number of degrees of freedom, and Γ is the gamma function. We calculate the χ^2 statistic using the observational errors and an empirical covariance matrix,

$$\chi^2 = (f_i - m_i)(\text{COV}_{ij})^{-1}(f_j - m_j), \quad \text{(A18)}$$

where f_i are the observed fluxes and m_i are the integrated synthetic fluxes for the model. The covariance matrix COV_{ij} is calculated using the observational errors σ_i and an empirical covariance calculated over the hydrodynamical simulation sample:

$$\text{COV} = 1.5\text{COV}_{sys} + \frac{1}{\boldsymbol{\sigma}^2_{obs}}, \quad \text{(A19)}$$

$$\text{COV}_{sys,ij} = \langle r_i r_j \rangle - \langle r_i \rangle \langle r_j \rangle;\ r_i = f_i - m_i. \quad \text{(A20)}$$

Here σ_i includes a 10% systematic error to account for cross-instrument calibration, and we scale COV_{sys} by a factor of 1.5 to account for the theoretical uncertainty, assumed to have the same covariance structure as the theoretical calibration uncertainty. This covariance matrix is constructed for every SN data set separately. For every SN, a synthetic data set is created using the sampling and bands available in its individual data set. The average is calculated over the parameter space of valid models (i.e., where $t < t_{validity}$) for each data point.

A.2. Early-time Colors

The early-time colors of the SNe in our samples excluding the extinguished SN 2020fqv are shown in Table 5. The full ZTF *g* and *r* light curves are shown in Figure 23.

ORCID iDs

Ido Irani https://orcid.org/0000-0002-7996-8780
Avishay Gal-Yam https://orcid.org/0000-0002-3653-5598
Eli Waxman https://orcid.org/0000-0002-9038-5877

Steve Schulze https://orcid.org/0000-0001-6797-1889
Jesper Sollerman https://orcid.org/0000-0003-1546-6615
Daniel A. Perley https://orcid.org/0000-0001-8472-1996
Ping Chen https://orcid.org/0000-0003-0853-6427
Nora L. Strotjohann https://orcid.org/0000-0002-4667-6730
Ofer Yaron https://orcid.org/0000-0002-0301-8017
Erez A. Zimmerman https://orcid.org/0000-0001-8985-2493
Rachel Bruch https://orcid.org/0000-0001-8208-2473
Eran O. Ofek https://orcid.org/0000-0002-6786-8774
Maayane T. Soumagnac https://orcid.org/0000-0001-6753-1488
Yi Yang https://orcid.org/0000-0002-6535-8500
Steven L. Groom https://orcid.org/0000-0001-5668-3507
Frank J. Masci https://orcid.org/0000-0002-8532-9395
Reed Riddle https://orcid.org/0000-0002-0387-370X
Eric C. Bellm https://orcid.org/0000-0001-8018-5348

References

Arcavi, I., Gal-Yam, A., Yaron, O., et al. 2011, ApJL, 742, L18
Astropy Collaboration, Price-Whelan, A. M., Sipőcz, B. M., et al. 2018, AJ, 156, 123
Astropy Collaboration, Robitaille, T. P., Tollerud, E. J., et al. 2013, A&A, 558, A33
Barbary, K. 2016, extinction v0.3.0, Zenodo, doi:10.5281/zenodo.804967
Baron, E., Branch, D., Hauschildt, P. H., et al. 2000, ApJ, 545, 444
Bellm, E. C., Kulkarni, S. R., Graham, M. J., et al. 2019, PASP, 131, 018002
Ben-Ami, S., Gal-Yam, A., Mazzali, P. A., et al. 2014, ApJ, 785, 37
Bersten, M. C., Folatelli, G., García, F., et al. 2018, Natur, 554, 497
Bertin, E., 2010 SWarp: Resampling and Co-adding FITS Images Together, Astrophysics Source Code Library, ascl:1010.068
Blagorodnova, N., Neill, J. D., Walters, R., et al. 2018, PASP, 130, 035003
Blinnikov, S., Lundqvist, P., Bartunov, O., Nomoto, K., & Iwamoto, K. 2000, ApJ, 532, 1132
Boian, I., & Groh, J. H. 2019, A&A, 621, A109
Bostroem, K. A., Dessart, L., Hillier, D. J., et al. 2023a, ApJL, 953, L18
Bostroem, K. A., Pearson, J., Shrestha, M., et al. 2023b, ApJL, 956, L5
Breeveld, A. A., Landsman, W., Holland, S. T., et al. 2011, in AIP Conf. Ser. 1358, Gamma Ray Bursts 2010, ed. J. E. McEnery, J. L. Racusin, & N. Gehrels (Melville, NY: AIP), 373
Brown, P. J., Breeveld, A., Roming, P. W. A., & Siegel, M. 2016, AJ, 152, 102
Brown, P. J., Dessart, L., Holland, S. T., et al. 2007, ApJ, 659, 1488
Bruch, R. J., Gal-Yam, A., Schulze, S., et al. 2021, ApJ, 912, 46
Bruch, R. J., Gal-Yam, A., Yaron, O., et al. 2023, ApJ, 952, 119
Burrows, D. N., Hill, J. E., Nousek, J. A., et al. 2005, SSRv, 120, 165
Calzetti, D., Armus, L., Bohlin, R. C., et al. 2000, ApJ, 533, 682
Cardelli, J. A., Clayton, G. C., & Mathis, J. S. 1989, ApJ, 345, 245
Cenko, S. B., Fox, D. B., Moon, D.-S., et al. 2006, PASP, 118, 1396
Chambers, K. C., Magnier, E. A., Metcalfe, N., et al. 2016, arXiv:1612.05560
Chevalier, R. A. 1992, ApJ, 394, 599
Chevalier, R. A., & Fransson, C. 1994, ApJ, 420, 268
Chevalier, R. A., & Irwin, C. M. 2011, ApJL, 729, L6
Chevalier, R. A., & Irwin, C. M. 2012, ApJL, 747, L17
Coughlin, M. W., Bloom, J. S., Nir, G., et al. 2023, ApJS, 267, 31
Dahiwale, A., & Fremling, C. 2020a, Transient Name Server Classification Report 2020-2576
Dahiwale, A., & Fremling, C. 2020b, Transient Name Server Classification Report 2020-3837
Davies, B., Crowther, P. A., & Beasor, E. R. 2018, MNRAS, 478, 3138
Davies, B., Kudritzki, R.-P., Plez, B., et al. 2013, ApJ, 767, 3
de Jager, C., Nieuwenhuijzen, H., & van der Hucht, K. A. 1988, A&AS, 72, 259
Deckers, M., Prentice, S., Maguire, K., et al. 2021, Transient Name Server Classification Report 2021-1376
Dekany, R., Smith, R. M., Riddle, R., et al. 2020, PASP, 132, 038001
Delgado, M., Galbany, L., Gonzalez, R., Munoz, S., & Zimmerman, E. 2021, Transient Name Server Classification Report 2021-202
Dessart, L., & Hillier, D. J. 2019, A&A, 625, A9
Dessart, L., Hillier, D. J., & Audit, E. 2017, A&A, 605, A83
Efron, B., & Tibshirani, R. J. 1993, An Introduction to the Bootstrap, Monographs on Statistics and Applied Probability No. 57 (Boca Raton, Florida: Chapman & Hall),
Evans, P. A., Beardmore, A. P., Page, K. L., et al. 2007, A&A, 469, 379
Evans, P. A., Beardmore, A. P., Page, K. L., et al. 2009, MNRAS, 397, 1177
Faran, T., Nakar, E., & Poznanski, D. 2017, MNRAS, 473, 513
Feroz, F., Hobson, M. P., & Bridges, M. 2009, MNRAS, 398, 1601
Förster, F., Moriya, T. J., Maureira, J. C., et al. 2018, NatAs, 2, 808
Fransson, C., Lundqvist, P., & Chevalier, R. A. 1996, ApJ, 461, 993
Fremling, C., Miller, A. A., Sharma, Y., et al. 2020, ApJ, 895, 32
Fremling, C., Sollerman, J., Taddia, F., et al. 2016, A&A, 593, A68
Gall, E. E. E., Polshaw, J., Kotak, R., et al. 2015, A&A, 582, A3
Gal-Yam, A. 2017, in Handbook of Supernovae, ed. A. W. Alsabti & P. Murdin (Berlin: Springer), 195
Gal-Yam, A., Arcavi, I., Ofek, E. O., et al. 2014, Natur, 509, 471
Gal-Yam, A., Bruch, R., Schulze, S., et al. 2022, Natur, 601, 201
Gal-Yam, A., Kasliwal, M. M., Arcavi, I., et al. 2011, ApJ, 736, 159
Gal-Yam, A., Leonard, D. C., Fox, D. B., et al. 2007, ApJ, 656, 372
Ganot, N., Ofek, E. O., Gal-Yam, A., et al. 2022, ApJ, 931, 71
Garnavich, P. M., Tucker, B. E., Rest, A., et al. 2016, ApJ, 820, 23
Gehrels, N., Chincarini, G., Giommi, P., et al. 2004, ApJ, 611, 1005
Goldberg, J. A., Bildsten, L., & Paxton, B. 2019, ApJ, 879, 3
Goldberg, J. A., Jiang, Y.-F., & Bildsten, L. 2022a, ApJ, 929, 156
Goldberg, J. A., Jiang, Y.-F., & Bildsten, L. 2022b, ApJ, 933, 164
González-Gaitán, S., Tominaga, N., Molina, J., et al. 2015, MNRAS, 451, 2212
Graham, M. J., Kulkarni, S. R., Bellm, E. C., et al. 2019, PASP, 131, 078001
Grefenstette, B. W., Brightman, M., Earnshaw, H. P., Harrison, F. A., & Margutti, R. 2023, ApJL, 952, L3
Hachinger, S., Mazzali, P. A., Taubenberger, S., Pakmor, R., & Hillebrandt, W. 2009, MNRAS, 399, 1238
HI4PI Collaboration, Ben Bekhti, N., Flöer, L., et al. 2016, A&A, 594, A116
Higson, E., Handley, W., Hobson, M., & Lasenby, A. 2019, Statistics and Computing, 29, 891
Hillier, D. J., & Dessart, L. 2019, A&A, 631, A8
Hiramatsu, D., Arcavi, I., Zimmerman, E., et al. 2020, Transient Name Server Classification Report 2020-1922
Hiramatsu, D., Howell, D. A., Van Dyk, S. D., et al. 2021, NatAs, 5, 903
Hiramatsu, D., Tsuna, D., Berger, E., et al. 2023, ApJL, 955, L8
Ho, A. Y. Q., Goldstein, D. A., Schulze, S., et al. 2019, ApJ, 887, 169
Hosseinzadeh, G., Farah, J., Shrestha, M., et al. 2023, ApJL, 953, L16
Hosseinzadeh, G., Kilpatrick, C. D., Dong, Y., et al. 2022, ApJ, 935, 31
Hosseinzadeh, G., Valenti, S., McCully, C., et al. 2018, ApJ, 861, 63
Hunter, J. D. 2007, CSE, 9, 90
Immler, S., & Brown, P. J. 2012, ATel, 3995, 1
Irani, I., Chen, P., Morag, J., et al. 2024a, ApJ, 962, 109
Irani, I., Morag, J., & Soumagnac, M. 2024b, SNeSCOPE - a python package for shock cooling fitting using the model of Morag et al 2024, v1, Zenodo, doi:10.5281/zenodo.10909914
Itagaki, K. 2023, Transient Name Server Discovery Report 2023-1158
Jacobson-Galán, W. V., Dessart, L., Jones, D. O., et al. 2022, ApJ, 924, 15
Jacobson-Galán, W. V., Dessart, L., Margutti, R., et al. 2023, ApJL, 954, L42
Jones, D. O., Foley, R. J., Narayan, G., et al. 2021, ApJ, 908, 143
Kasliwal, M. M., Cannella, C., Bagdasaryan, A., et al. 2019, PASP, 131, 038003
Katz, B., Kushnir, D., & Dong, S. 2013, arXiv:1301.6766
Katz, B., Sapir, N., & Waxman, E. 2011, in IAU Proc. 279, Death of Massive Stars: Supernovae and Gamma-Ray Bursts, 274
Katz, B., Sapir, N., & Waxman, E. 2012, ApJ, 747, 147
Khazov, D., Yaron, O., Gal-Yam, A., et al. 2016, ApJ, 818, 3
Kulkarni, S. R. 2013, ATel, 4807, 1
Law, N. M., Kulkarni, S. R., Dekany, R. G., et al. 2009, PASP, 121, 1395
Li, G., Hu, M., Li, W., et al. 2024, Natur, 627, 754
Margutti, R., Chakraborti, S., Brown, P. J., & Sokolovsky, K. 2013, ATel, 5243, 1
Marshall, J. R., van Loon, J. T., Matsuura, M., et al. 2004, MNRAS, 355, 1348
Masci, F. J., Laher, R. R., Rusholme, B., et al. 2019, PASP, 131, 018003
Matzner, C. D., & McKee, C. F. 1999, ApJ, 510, 379
Modjaz, M., Gutiérrez, C. P., & Arcavi, I. 2019, NatAs, 3, 717
Morag, J., Irani, I., Sapir, N., & Waxman, E. 2024, MNRAS, 528, 7137
Morag, J., Sapir, N., & Waxman, E. 2023, MNRAS, 522, 2764
Morozova, V., Piro, A. L., & Valenti, S. 2018, ApJ, 858, 15
Mould, J. R., Huchra, J. P., Freedman, W. L., et al. 2000, ApJ, 529, 786
Nakar, E., & Sari, R. 2010, ApJ, 725, 904
Nugent, P. E., Sullivan, M., Cenko, S. B., et al. 2011, Natur, 480, 344
Ofek, E. O., Rabinak, I., Neill, J. D., et al. 2010, ApJ, 724, 1396
Ofek, E. O., Zoglauer, A., Boggs, S. E., et al. 2014, ApJ, 781, 42
Harris, C. R., Millman, K. J., van der Walt, S., et al. 2020, Natur, 585, 357
Perez, F., & Granger, B. E. 2007, CSE, 9, 21

Perley, D. 2019, Transient Name Server Classification Report 2019-2715
Perley, D. A., Fremling, C., Sollerman, J., et al. 2020b, ApJ, 904, 35
Perley, D. A., Sollerman, J., Schulze, S., et al. 2022, ApJ, 927, 180
Perley, D. A., Taggart, K., Dahiwale, A., & Fremling, C. 2020a, Transient Name Server Classification Report 2020-2086
Pessi, P., Anderson, J., Gutierrez, C., & Irani, I. 2020, Transient Name Server Classification Report 2020-3798
Phillips, M. M., Lira, P., Suntzeff, N. B., et al. 1999, AJ, 118, 1766
Piro, A. L. 2015, ApJL, 808, L51
Piro, A. L., Haynie, A., & Yao, Y. 2021, ApJ, 909, 209
Planck Collaboration, Aghanim, N., Akrami, Y., et al. 2018, A&A, 641, A6
Qin, Y.-J., Zhang, K., Bloom, J., et al. 2023, arXiv:2309.10022
Rabinak, I., & Waxman, E. 2011, ApJ, 728, 63
Ricker, G. R., Winn, J. N., Vanderspek, R., et al. 2014, Proc. SPIE, 9143, 914320
Rodrigo, C., & Solano, E. 2020, in XIV.0 Scientific Meeting (virtual) of the Spanish Astronomical Society, 182
Rodrigo, C., Solano, E., & Bayo, A. 2012, SVO Filter Profile Service Version 1.0 IVOA Working Draft 15 October 2012, 10.5479/ADS/bib/2012ivoa.rept.1015R
Roming, P. W. A., Kennedy, T. E., Mason, K. O., et al. 2005, SSRv, 120, 95
Rubin, A., & Gal-Yam, A. 2017, ApJ, 848, 8
Rubin, A., Gal-Yam, A., Cia, A. D., et al. 2016, ApJ, 820, 33
Salim, S., & Narayanan, D. 2020, ARA&A, 58, 529
Sapir, N., & Halbertal, D. 2014, ApJ, 796, 145
Sapir, N., Katz, B., & Waxman, E. 2011, ApJ, 742, 36
Sapir, N., Katz, B., & Waxman, E. 2013, ApJ, 774, 79
Sapir, N., & Waxman, E. 2017, ApJ, 838, 130
Saxton, R. D., König, O., Descalzo, M., et al. 2022, A&C, 38, 100531
Schlafly, E. F., & Finkbeiner, D. P. 2011, ApJ, 737, 103
Schlegel, D. J., Finkbeiner, D. P., & Davis, M. 1998, ApJ, 500, 525
Shvartzvald, Y., Waxman, E., Gal-Yam, A., et al. 2024, ApJ, 964, 74
Siebert, M. R., Davis, K., Tinyanont, S., Foley, R. J., & Strasburger, E. 2021, Transient Name Server Classification Report 2021-2383
Skilling, J. 2004, in AIP Conf. Ser. 735, Bayesian Inference and Maximum Entropy Methods in Science and Engineering, ed. R. Fischer, R. Preuss, & U. V. Toussaint (Melville, NY: AIP), 395
Skilling, J. 2006, BayAn, 1, 833
Smartt, S. J. 2009, ARA&A, 47, 63
Smartt, S. J. 2015, PASA, 32, e016
Smith, J. A., Tucker, D. L., Kent, S., et al. 2002, AJ, 123, 2121
Sollerman, J., Yang, S., Schulze, S., et al. 2021, A&A, 655, A105
Soumagnac, M. T., Ganot, N., Irani, I., et al. 2020, ApJ, 902, 6
Speagle, J. S. 2020, MNRAS, 493, 3132
Steele, I. A., Smith, R. J., Rees, P. C., et al. 2004, Proc. SPIE, 5489, 679
Stritzinger, M. D., Taddia, F., Burns, C. R., et al. 2018, A&A, 609, A135
Svirski, G., Nakar, E., & Sari, R. 2012, ApJ, 759, 108
Tartaglia, L., Sand, D. J., Valenti, S., et al. 2018, ApJ, 853, 62
Terreran, G., Jacobson-Galán, W. V., Groh, J. H., et al. 2022, ApJ, 926, 20
Tinyanont, S., Ridden-Harper, R., Foley, R. J., et al. 2022, MNRAS, 512, 2777
Tonry, J. L., Denneau, L., Heinze, A. N., et al. 2018, PASP, 130, 064505
Valenti, S., Howell, D. A., Stritzinger, M. D., et al. 2016, MNRAS, 459, 3939
Valerin, G., Pumo, M. L., Pastorello, A., et al. 2022, MNRAS, 513, 4983
Vallely, P. J., Kochanek, C. S., Stanek, K. Z., Fausnaugh, M., & Shappee, B. J. 2021, MNRAS, 500, 5639
van der Walt, S., Crellin-Quick, A., & Bloom, J. 2019, JOSS, 4, 1247
Van Dyk, S. D. 2017, RSPTA, 375, 20160277
van Loon, J. T., Cioni, M. R. L., Zijlstra, A. A., & Loup, C. 2005, A&A, 438, 273
Vasylyev, S. S., Filippenko, A. V., Vogl, C., et al. 2022, ApJ, 934, 134
Vasylyev, S. S., Vogl, C., Yang, Y., et al. 2023, ApJL, 959, L26
Vasylyev, S. S., Yang, Y., Patra, K. C., et al. 2024, MNRAS, 527, 3106
Virtanen, P., Gommers, R., Oliphant, T. E., et al. 2020, NatMe, 17, 261
Waxman, E., & Katz, B. 2017, in Handbook of Supernovae, ed. A. W. Alsabti & P. Murdin (Berlin: Spring), 967
Weil, K. E., Subrayan, B. M., & Milisavljevic, D. 2020, Transient Name Server Classification Report 2020-3912
Yang, S., Sollerman, J., Strotjohann, N. L., et al. 2021, A&A, 655, A90
Yaron, O., & Gal-Yam, A. 2012, PASP, 124, 668
Yaron, O., Perley, D. A., Gal-Yam, A., et al. 2017, NatPh, 13, 510
York, D. G., Adelman, J., Anderson, J. E., Jr, et al. 2000, AJ, 120, 1579
Zackay, B., Ofek, E. O., & Gal-Yam, A. 2016, ApJ, 830, 27
Zimmerman, E. A., Irani, I., Chen, P., et al. 2024, Natur, 627, 759